

Hydrodynamics of water-worked and screeded gravel beds: A comparative study

Ellora Padhi^{1,a}, Nadia Penna^{2,b}, Subhasish Dey^{1,c}, and Roberto Gaudio^{2,d}

¹ *Department of Civil Engineering, Indian Institute of Technology Kharagpur, West Bengal 721302, India*

² *Dipartimento di Ingegneria Civile, Università della Calabria, 87036 Rende (CS), Italy*

The turbulence characteristics within flows over water-worked (WGB) and screeded gravel beds (SGB) were examined by measuring the instantaneous flow velocity field using a two-dimensional particle image velocimetry system. To compare the responses of a WGB and an SGB to velocity and various turbulence characteristics, the flow Froude number was kept identical for both the beds that remained immobile. The roughness structures of both the beds were measured using a laser scanner. The results showed that the bed surface roughness was higher in the WGB than in the SGB. However, the longest axis of WGB gravels were oriented streamwise owing to the action of water work, but SGB gravels were randomly poised. The distribution of bed roughness fluctuations was negatively skewed in the WGB and positively skewed in the SGB. Double averaging methodology was applied to analyze the flow parameters. In this paper, the vertical profiles of the double-averaged (DA) streamwise velocity and the turbulence parameters, specifically the spatially averaged (SA) Reynolds shear and normal stresses, form-induced shear and normal stresses, turbulent kinetic energy (TKE) and form-induced TKE fluxes, quadrant analysis of SA Reynolds shear stress, etc., are presented and analyzed critically by focusing on comparisons between a WGB and an SGB. Comparative study reveals that in the near-bed flow zone, the SGB underestimates the turbulence parameters compared to the WGB. Therefore, in order to represent the prototypical flow in laboratory, the experiments should be performed in a WGB.

I. INTRODUCTION

Flow over a gravel bed, especially in the near-bed flow zone, has been of continued research interest for several decades owing to its practical importance.¹⁻⁸ Gravel-bed flow is heavily influenced by colossal fluid-particle interactions, such as wake flow downstream of gravels, accelerated flow over gravel crests, and decelerated flow in interstices of gravels. These complex fluid-particle interactions give rise to spatial flow heterogeneities and are to enhance temporal intermittency in the near-bed flow.⁹⁻¹³ It is therefore important to understand the turbulent flow

^{a)} ellora@iitkgp.ac.in

^{b)} nadia.penna@unical.it

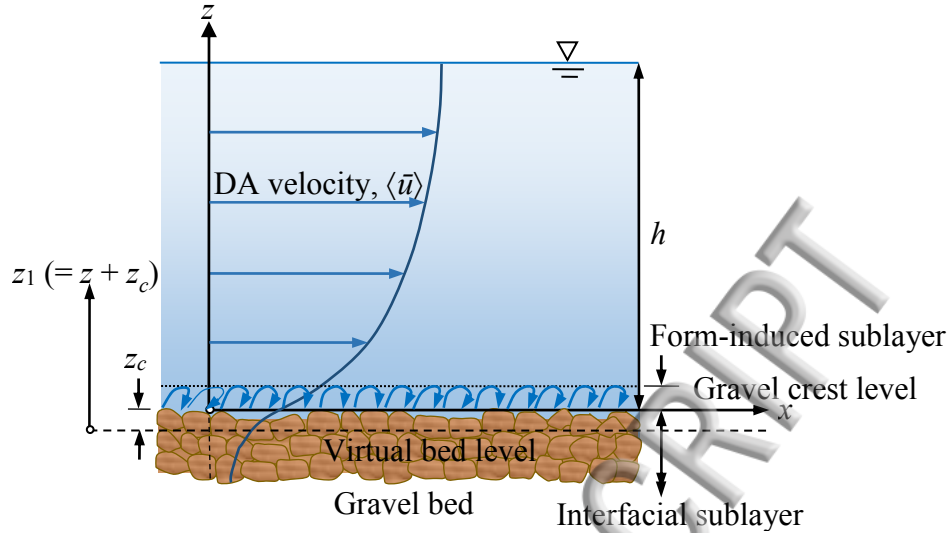
^{c)} sdey@iitkgp.ac.in

^{d)} Author to whom correspondence should be addressed. Electronic mail: gaudio@unical.it

39 characteristics that arise from these complex turbulence mechanisms by resolving spatial flow
40 heterogeneities. This enables us to accurately estimate the resistance to a hydraulically macro-
41 rough flow (e.g. a mountainous river flow over a gravelly or a bouldery bed) and/or to predict the
42 particle transport rate. In a natural river, the flow velocity plays a significant role in developing
43 the bed surface topography formed by various roughness elements. Specifically, the gravels at
44 the bed surface move if the flow velocity exceeds the threshold velocity for gravel motion. Thus,
45 the surface topography of a natural gravel bed exhibits spatially multifaceted, three-dimensional
46 organization (orientation, alignment, spacing, and clustering of the gravel deposits), because it is
47 created by transport processes as a result of continual deposition and reworking by several flood
48 cycles. In this way, a so-called *water-worked gravel bed* (WGB) is formed in a natural river.

49 In contrast, laboratory experimental flume studies typically use a simulated gravelly riverbed
50 that is prepared by randomly depositing mixed gravels into the flume to reach a given thickness.
51 The gravel-bed surface is then scraped and leveled, forming a *screeded gravel bed* (SGB). The
52 statistical distributions in terms of bed surface topography of an SGB are unable to appropriately
53 represent a WGB, even though the bed surface formed by the gravels has the same particle size
54 distribution. The WGB can however be produced in a laboratory flume transporting the gravel
55 deposits by the flow. Notably the laboratory gravel bed can be deemed acceptable provided that
56 the orientation, alignment, spacing, and clustering of gravels are analogous to the conditions in
57 the prototype and that the distribution of the scaled gravel size is similar to that of the natural
58 gravel bed. Importantly, the signature of bed roughness characteristic is effectively transmitted to
59 the time-averaged flow characteristics, turbulence parameters, and resistance to flow.

60 Although extensive experimental studies on rough-bed flow have been performed, most have
61 used SGBs. SGB surface topographies are quite different from those of natural gravel riverbeds.
62 Only a handful of researchers performed experimental studies on WGBs, which more closely
63 resemble natural gravel beds. Cooper and Tait¹⁴ and Hardy *et al.*¹⁵ performed various
64 experiments and concluded that the time-averaged flow over a WGB is spatially heterogeneous
65 and strongly influenced by the relative submergence. Further, Cooper and Tait¹⁶ performed
66 experiments using both WGBs and SGBs to examine the spatial features of time-averaged
67 streamwise velocity in the near-bed flow zone. They observed that the distribution of bed surface
68 fluctuations was almost symmetric and positively skewed in a WGB, but negatively skewed in
69 an SGB. Furthermore, the standard deviation of the bed surface fluctuations in a WGB was
70 found to be higher than that in an SGB. The effects of the bed surface geometry and roughness
71 were reflected by the differences between the flow characteristics over the WGB and SGB. Other
72 researchers also studied turbulent flow characteristics over WGBs in order to explore the effects
73 of bed roughness on the streamwise velocity, Reynolds shear stress (RSS), Reynolds normal
74 stresses, and form-induced shear stress profiles.^{17–22} Despite these experimental studies, a
75 detailed turbulence analysis that compares the higher-order turbulence statistics (i.e., turbulent
76 kinetic energy (TKE) flux and form-induced TKE flux), conditional RSS, and specific temporal
77 flow pictures of WGBs and SGBs is not available.



78
79

80 FIG. 1. Schematic of turbulent flow over a macro-rough bed with flow sublayers.

81

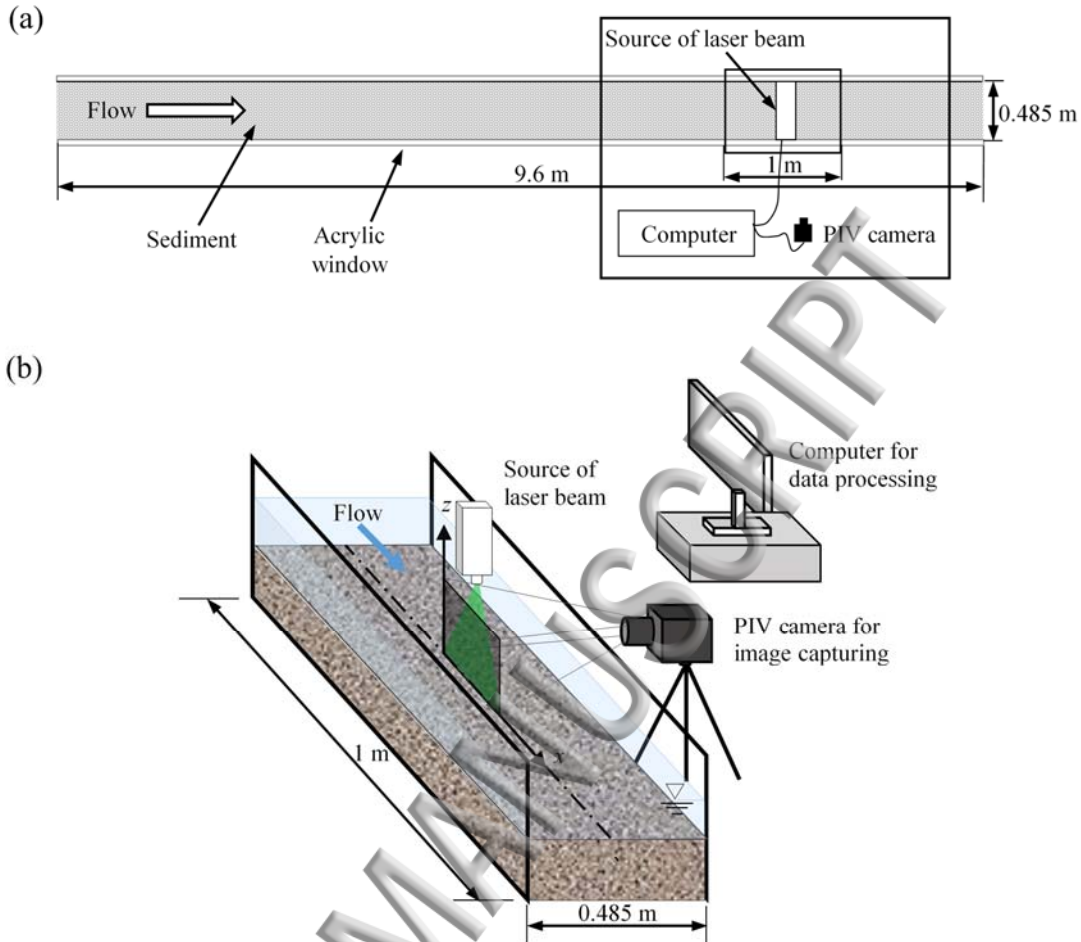
82 Further in order to resolve the spatial flow heterogeneity, area averaging of the time-averaged
83 quantities is performed over the layer parallel to the mean bed surface, called the *double-*
84 *averaging methodology* (DAM).^{23–27} In DAM, the local time-averaged quantity $\bar{\theta}$ is
85 decomposed as $\bar{\theta} = \langle \bar{\theta} \rangle + \tilde{\theta}$, where $\tilde{\theta}$ is the fluctuations in $\bar{\theta}$ with respect to the double-
86 averaged (DA) quantity $\langle \bar{\theta} \rangle$. By Reynolds decomposition, an instantaneous quantity θ is given
87 by $\theta = \bar{\theta} + \theta'$, where θ' is the fluctuations in θ with respect to $\bar{\theta}$. Here, the angle bracket $\langle - \rangle$
88 indicates the intrinsic spatial average. Below the crest of roughness elements, a roughness
89 geometry function $\phi(z) (= A_f/A_0)$ that contributes to a superficial DA flow is introduced as a
90 multiplier of the intrinsic DA flow quantity $\langle \bar{\theta} \rangle$.⁸ Here, $A_f(z)$ is the fluid-occupied area at an
91 elevation z below the crest ($z < 0$, where z has an origin at the crest and is positive above the
92 crest) and A_0 is the total area over which the average is calculated. The roughness layer is divided
93 into two sublayers: the form-induced and interfacial sublayers (Fig. 1). The form-induced
94 sublayer is the flow region between the top of the roughness layer and the roughness crest, while
95 the interfacial sublayer is the flow region below the crest. These sublayers are influenced by
96 individual roughness elements.

97 The aim of this study was therefore to examine the spatially averaged (SA) turbulent flow
98 characteristics over a WGB and an SGB prepared using the same gravel samples. This paper thus
99 highlights how the bed surface topography of a WGB influences the turbulence characteristics in
100 the near-bed flow zone differently from that of an SGB when the same gravels and flow
101 conditions are used. It therefore provides improved descriptions of the differences between WGB
102 and SGB turbulence characteristics such as the DA streamwise velocity, SA RSS, Reynolds
103 normal stresses, TKE flux, RSS quadrant analysis, form-induced shear stress, form-induced
104 normal stresses, etc. However, the flow characteristics were measured only in the vertical plane
105 along the streamwise direction, because a two-dimensional particle image velocimetry (PIV)
106 system was employed.

107

108 II. EXPERIMENTAL APPARATUS AND PROCEDURE

109



110
111

112 FIG. 2. Schematic of (a) the experimental apparatus (plan view) and (b) the flume test section
113 showing the laser pulser and PIV camera (both connected to a synchronizer to aid in capturing
114 frames produced during laser emission), as well as the computer used for data processing.

115

116 Experiments were performed in the *Grandi Modelli Idraulici* laboratory at the Università della
117 Calabria, Italy. A 9.6 m long, 0.485 m wide, 0.5 m deep rectangular tilting flume was used. The
118 inlet of the flume consisted of a stilling tank, an uphill slipway, and a honeycomb designed to
119 dampen the flow disturbances. The flow depth in the flume was regulated by adjusting the
120 downstream tailgate. A tank was attached downstream of the tailgate to collect the outflow. A
121 gravel trap was placed over the tank to collect transported gravel particles. The flow discharge in
122 the flume was metered using a calibrated Thomson weir fitted at the outlet of the tank. The
123 experimental bed was prepared using coarse gravels with a unimodal size distribution ($4 < d < 6$
124 mm) having a median size of $d_{50} = 4.81$ mm. The geometric standard deviation $\sigma_g (= (d_{84}/d_{16})^{0.5})$
125 of the gravel sample was 1.18 (< 1.4), which indicates that the gravel particles were uniform. The
126 gravels were considerably non-spherical (approximately elliptical cross-section tapering toward
127 each end), having the average longest, intermediate and shortest axial lengths of individual
128 gravels of $a = 12.3$ mm, $b = 5.9$ mm and $c = 4.5$ mm, respectively. The flume walls were made of
129 glass enabling to visualize the flow. All measurements were taken within a 1 m long zone 6.3 m
130 to 7.3 m from the flume inlet. To ensure the fully developed flow, the flow development length
131 was calculated from the boundary layer thickness formula²⁸ ($\delta = 0.33 xu^*/U$, where x is the

streamwise distance, u^* is the shear velocity, and U is the maximum flow velocity) and found to be 2.24 m from the inlet. In addition, the velocity profiles within the test section were found to be fully developed, which confirmed the fully developed flow in the test section. Furthermore, the uniformity of flow in the test section was ascertained by measuring the flow profile with a point gauge. During flow measurements for both the WGB and SGB, the flow depths were maintained same by regulating the adjustable downstream tailgate. Thus, the flow Froude numbers were identical. A schematic diagram of the experimental flume and instruments is shown in Fig. 2(a).

The flow field over the gravel bed was measured using a two-dimensional (2D) particle image velocimetry system manufactured by TSI (Fig. 2(b)). It consisted of a Nikon 12-bit charge-coupled device (CCD) camera, model 630091 POWERVIEW Plus 4M, with 2048×2048 square pixels and a frame rate of 15 Hz, as well as a double-pulse Nd:YAG laser, model EverGreen 200 manufactured by Quantel, with a pulse energy of 200 mJ at wavelength of 532 nm. The Laser pulser and the camera were synchronized by a LaserPulse Synchronizer Model 610036. Two (one spherical and one cylindrical) lenses were attached to the laser head nozzle to illuminate the flow with a light sheet having a thickness of 2 mm. Although the PIV system used in this study can work at 15 Hz, it was operated at 7.25 Hz owing to a PC port frequency limitation. Further, the double-frame mode was used to achieve a satisfactory spatiotemporal resolution, where two images were captured within a very short time equaling 1000 μ s. This inter-frame time (time delay) between the two laser pulses should be long enough for determining the displacement of the seeding particles in the pair of images with sufficient resolution. On the other hand, inter-frame time should be short enough to avoid particles with an out-of-plane velocity component leaving the laser sheet between subsequent pulses. It means that the inter-frame time was fixed to optimize the particle image displacement between the two captured frames according to the flow velocity. It was set during preliminary tests for the regulation of the amount of seeding particles to be used during the experiments. To discuss further, it follows that in the space domain, considering a mean flow velocity of 0.43 m s^{-1} and the fixed inter-frame time, we were able to measure only eddies greater than 0.43 mm. However, the actual size of the eddy was imposed by the spatial resolution of the PIV measurements. Having known the inter-frame time and computed the displacement of a seeding particle, the instantaneous velocity of the particle was estimated.

The INSIGHT 4G-2DTR software was used to control data acquisition and to process the resulting data. Titanium dioxide particles with a mean size of $3 \mu\text{m}$ and mass density of $4.26 \times 10^3 \text{ kg m}^{-3}$ were used as seeding particles and fed into the flow upstream. The seeding particles were fine enough to become ambient fluid particles even though their mass density was greater than that of water.^{29,30} Furthermore, care was taken to feed the seeding particles into the flow in a manner that satisfied the general criteria for an accurate PIV measurement.³¹ The laser sheet illuminated the test section in order to aid in visualizing the seeding particle motion captured by the camera placed parallel to the laser sheet.^{19,32,33} The base of the PIV camera was aligned parallel to the average bed level having an elevation of lens centerline (cross-hair) 5 cm from the average bed level (Fig. 2(b)),¹⁹ enabling us to identify the flow below the crest with no excessive reflection of the laser light from the bed surface. However, in some locations along the laser sheet, the camera visual field was to some extent blocked by some gravels immediate across the laser sheet.

The images were divided into several small rectangular frames called *interrogation areas* (IAs), was $170 \times 170 \text{ mm}^2$. No overlapping IAs were considered, as they would have increased

179 the computation time significantly without improving the results. During the experiments, the
180 laser sheet along with the camera was shifted to each measuring location, and then the flow
181 measurements were taken. Altogether 3000 pairs of images were captured on a vertical plane
182 along the flume centerline in order to measure the flow field over a period of 414 s at each
183 streamwise location, such as 0.06 m, 0.26 m, 0.46 m, 0.66 m, and 0.94 m from the starting point
184 of the test section. This duration of the test significantly exceeded that recommended for
185 measurements in boundary layer flow.^{34,35} The image particle size was less than 1 pixel. Thus, to
186 minimize the effect of peak locking, first of all the images were pre-processed by using a filter
187 (already available in the INSIGHT 4G-2DTR software), which optimized the particle image
188 diameter with respect to the peak estimator. This filter subtracted the background image of a
189 seeding particle (that is the fixed part of the image itself) in order to make more apparent the
190 moving seeding particles (that is the variable part) and to improve the signal to noise ratio. Then,
191 the Gaussian interpolation was used in order to determine the correlation peaks and the average
192 seeding particle displacement over an interrogation area with a sub-pixel accuracy. The image
193 analysis provided 43 velocity profiles on a vertical plane in the streamwise direction, covering an
194 area of $120 \times 100 \text{ mm}^2$ with a spatial resolution of 2.7 mm in both vertical and streamwise
195 directions at each measuring location. No data cleaning process was used in analyzing the data.

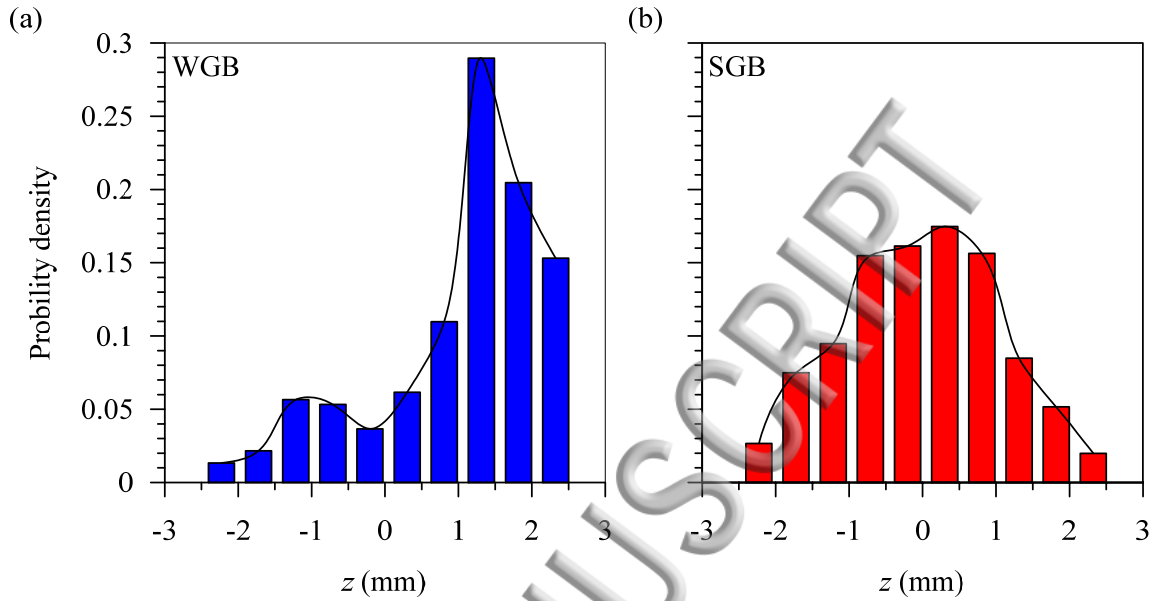
196 In the first phase, gravel particles were placed in the flume and screeded manually to form the
197 SGB and the bed surface fluctuations were measured using a laser scanner (Leica ScanStation
198 P20), having an accuracy of $\pm 3 \text{ mm}$ at 50 m and $\pm 6 \text{ mm}$ at 100 m. The average bed slope was
199 found to be 0.7%. Next, the WGB was produced by initiating flow over the SGB in a manner
200 that could transport the surface gravels. The flow depth h used to prepare the WGB was 0.088 m,
201 as measured from the gravel crest. The threshold flow velocity U_c needed to initiate bed-particle
202 motion was determined via Neill's³⁶ empirical formula to be 0.59 m s^{-1} . This is less than the
203 average flow velocity $U_{avg} (= Q/(Bh))$, where Q is the flow discharge and B is the flume width) of
204 0.82 m s^{-1} . Gravel transport rate (g_s) for the WGB preparation declined from $7.2 \times 10^{-2} \text{ kg m}^{-1}$
205 s^{-1} to $3 \times 10^{-4} \text{ kg m}^{-1} \text{ s}^{-1}$ over a period of 28.5 h because no gravel was fed. The flow was
206 stopped at the end of this phase. Then, the bed surface fluctuations were measured using the laser
207 scanner and the average bed slope was found to be 0.4%.

208 In the second phase, the flume was cleaned and the gravel particles were again placed in the
209 flume and manually screeded to create a new SGB. The bed slope of the new SGB was identical
210 to that of the earlier SGB ($= 0.7\%$) in order to understand the effects (before and after) of the
211 water-work on the flow characteristics and bed topographies. By analyzing the bed surface
212 fluctuations of the entire test section derived from the detrended laser scans of the bed
213 topography, the crests of gravels having the highest elevation, considered to be the crest level,
214 were obtained. Then they were compared with the lower boundary of the flow field obtained
215 from the PIV images.

216 From the bed surface fluctuations, the virtual bed levels (mean bed levels corresponding to $z =$
217 $-z_c$ or $z_1 = 0$, where z_c is the crest level) were computed for the WGB and SGB (Fig. 1). The
218 WGB and SGB gravel crest levels z_c ($z = 0$ or $z_1 = z_c$) were estimated to be 0.00196 m and
219 0.00283 m, respectively, above the virtual level. The average roughness heights Δk were
220 approximately equal to the standard deviations of the bed surface fluctuations. They were found
221 to be 1.25 mm and 1.04 mm for the WGB and SGB, respectively. These values can be
222 interpreted as the characteristic roughness of the two different beds.^{37,38} The bed surface
223 fluctuations measured along the WGB centerline that form the bed roughness follow an
asymmetric distribution with a skewness of -0.93 and a kurtosis of 3.26 (Fig. 3(a)). In contrast,

224 the fluctuations along the SGB centerline follow an asymmetric distribution with a skewness of
 225 0.04 and kurtosis of 2.41 (Fig. 3(b)).

226

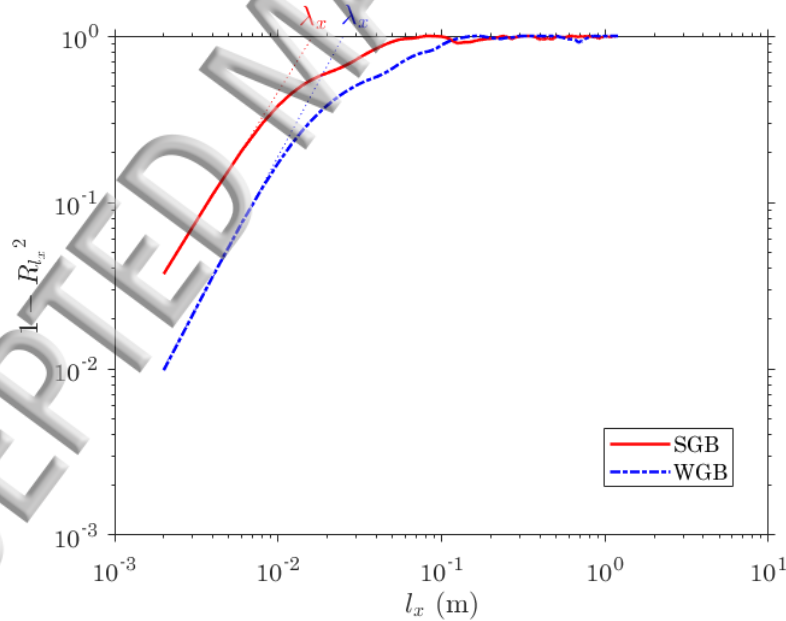


227

228

229 FIG. 3. The probability density functions and histograms of bed surface fluctuations as a function
 230 of mean surface elevation along the flume centerline in (a) the WGB and (b) the SGB.

231



232

233

234 FIG. 4. Autocorrelation functions at different spacing to determine horizontal length scales for
 235 the WGB and SGB.

236

237 The autocorrelation function R_{l_x} was calculated to determine the horizontal length scales λ_x for
 238 both the WGB and SGB (Fig. 4) as

240

$$R_{lx} = \frac{1}{N-n} \sum_{i=1}^{N-n} [z'(x_j)z'(x_j + n\delta x)], \quad (1)$$

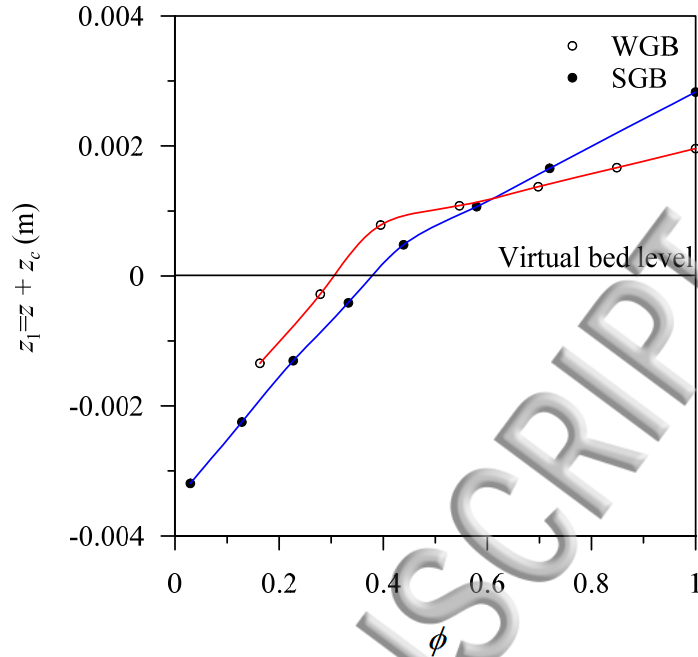
241

242 where l_x is the sampling length in x direction ($= n\delta x$), $i = 1, 2, 3, \dots, n$, n is the number of points in
 243 x direction, N is the total number of points in x direction, and δx is the sampling interval in x
 244 direction. In this study, we considered $\delta x = 2$ mm. The correlation length can be identified from
 245 the points with an intermediate distance l apart in which there exists a change of gradient of l in a
 246 data plot of $\log(1 - R_l^2)$ versus $\log(l)$.³⁹

247 It is possible to identify that the streamwise length scale λ_x for the WGB is smaller than that
 248 for the SGB, although the streamwise length scales for both the beds are larger than d_{50} . They are
 249 2.2×10^{-2} m and 1.7×10^{-2} m for the WGB and SGB, respectively. This trend demonstrates that the
 250 bed roughness structure is more elongated in x direction in the WGB than the SGB.

251 Flow measurements for WGB and SGB were taken with $h = 0.1$ m and $U_{avg} = 0.43$ m s⁻¹ $< U_c$
 252 ($= 0.6$ m s⁻¹). Since the threshold flow velocity was calculated to be 0.6 m s⁻¹ at $h = 0.1$ m using
 253 Neill's³⁶ formula, this indicates a clear-water condition. In recent past,^{8,23,32} accurate estimation
 254 of the u^* was achieved by extending the RSS profiles linearly to the roughness crest as $u^* (= -\langle$
 255 $\overline{u'w'}\rangle)^{0.5}|_{z=z_c}$). Therefore, in this study, the u^* in the WGB and SGB were obtained from the RSS
 256 profiles to be 0.068 m s⁻¹ and 0.077 m s⁻¹, respectively. In addition, using the bed slope method
 257 ($u^* = (ghS)^{0.5}$), the u^* values in the WGB and SGB were determined to be 0.063 m s⁻¹ and 0.083
 258 m s⁻¹, respectively. The percentage errors between two results were -7.3% and 7.8% for the
 259 WGB and SGB, respectively. Here, one can notice that the u^* in the WGB is smaller than that in
 260 the SGB, although the roughness in the former is higher than that in the latter. The reason is
 261 attributed to the lesser bed slope in the WGB than that in the SGB. The flow Reynolds number R
 262 ($= 4U_{avg}h/\nu$, where $\nu = 10^{-6}$ m² s⁻¹ at 20 °C) and flow Froude number Fr ($= U_{avg}/(gh)^{0.5}$, where g
 263 is the gravitational acceleration) were determined to be 1.72×10^5 and 0.432 , respectively. The
 264 shear particle Reynolds numbers R^* ($= u^* \Delta k/\nu$) in the WGB and SGB were calculated to be 85
 265 and 81, respectively. In both the cases, the values of R^* were greater than 70, which confirmed
 266 that the rough-turbulent flow prevailed. To ascertain the two-dimensionality of the flow field in
 267 the central part of the flume, flow measurements were performed at four different spanwise
 268 positions along the streamwise direction of the test section. Examination of the DA streamwise
 269 velocity and SA RSS profiles reveals that at least in the central portion of the flume (± 0.075 m
 270 off the centerline), the two-dimensionality of the flow was satisfactorily preserved.

271



272
273

274 FIG. 5. Variations of roughness geometry functions ϕ in the WGB and SGB with the vertical
275 distance $z_1 (= z + z_c)$.

276

277 For $z \leq 0$ (below the crest), the roughness geometry function ϕ was used as a multiplier to
278 convert the intrinsic DA flow quantity to a superficial DA flow quantity.^{8,40,41,42} The distributions
279 of the geometric function for the WGB and SGB are shown in Fig. 5.

280

281 III. RESULTS AND DISCUSSION

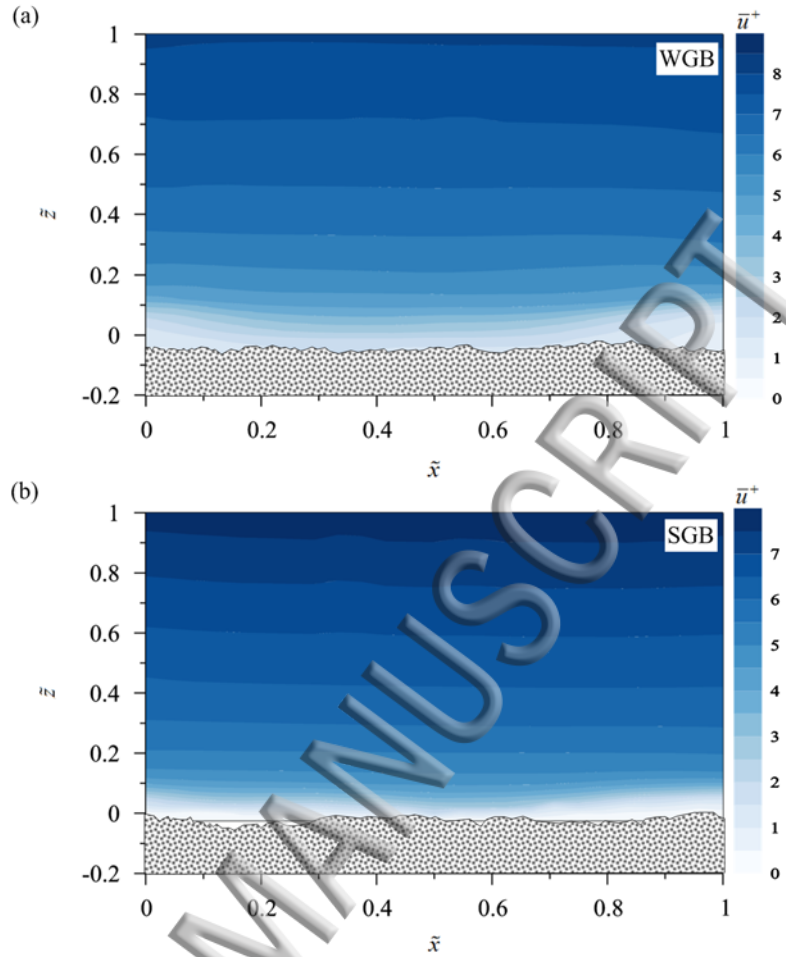
282

283 A. DA velocity

284

285 The contours of the dimensionless time-averaged velocities $\bar{u}^+ (= \bar{u}/u^*$, where \bar{u} is the time-
286 averaged streamwise velocity) on a central vertical plane in the WGB and SGB are shown in
287 Figs. 6(a) and 6(b), respectively. The horizontal and vertical axes of the contours in
288 dimensionless form are represented as $\tilde{x} (= x/L$, where L is the test section length) and $\tilde{z} (= z/h)$,
289 respectively. As is traditionally observed in a hydraulically rough flow, the flow velocities in
290 both the beds increase with the vertical distance z having streamwise spatial variations in the
291 near-bed flow zone owing to the roughness structures. It is evident that the near-bed flow
292 velocity in the SGB is influenced by the randomly poised roughness elements. On the other
293 hand, the near-bed flow in the WGB is roughly streamlined over the organized roughness
294 structure formed by gravels with their longest axis oriented streamwise owing to water work,
295 although the WGB roughness size is higher than the SGB roughness size.

296



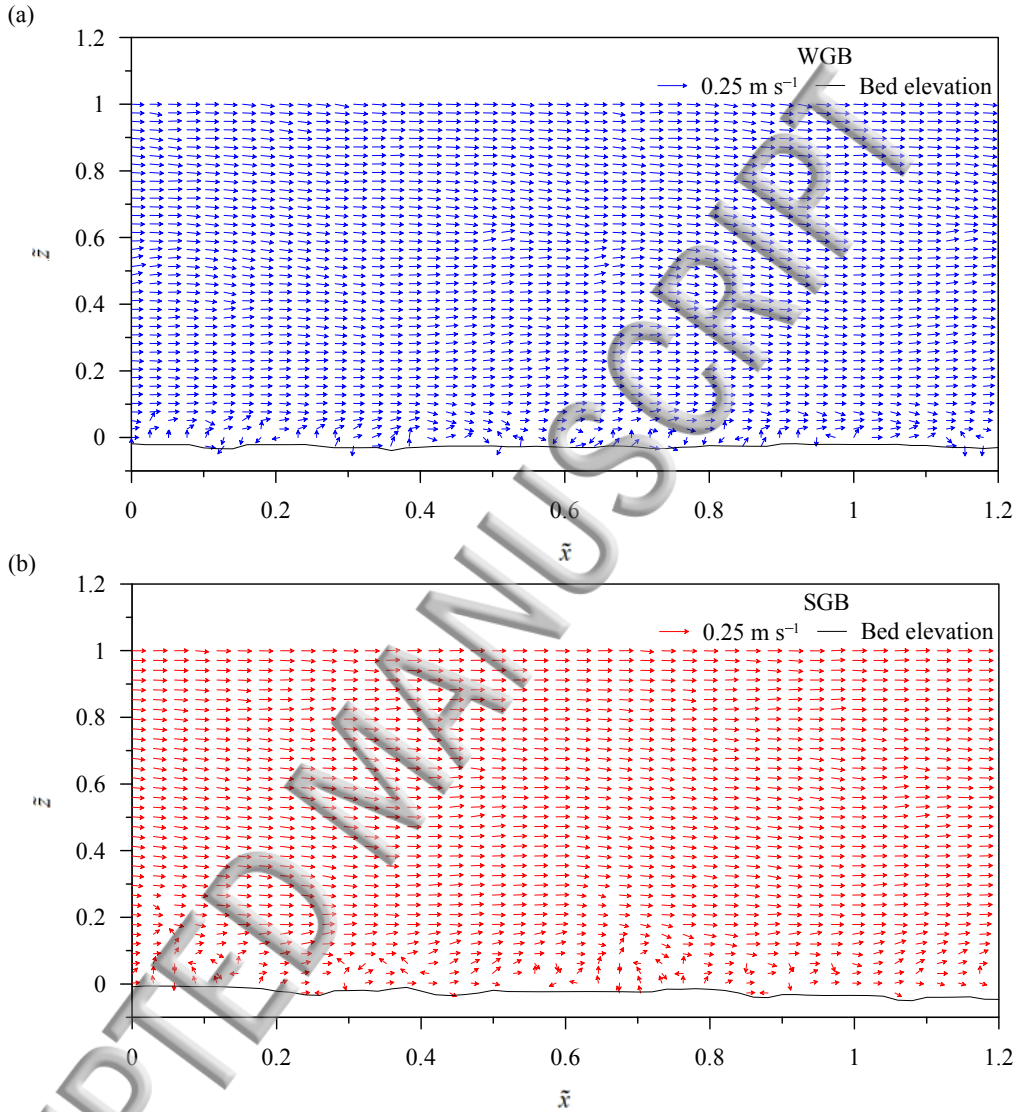
297
298

299 FIG. 6. Dimensionless time-averaged velocity \bar{u}^+ contours on a plane along the flume centerline
300 in (a) the WGB and (b) the SGB.

301

302 In order to substantiate the near-bed flow heterogeneity, the instantaneous velocity vectors are
303 plotted in Figs. 7(a) and 7(b) for the WGB and SGB, respectively. It is apparent that the near-bed
304 velocity vectors in the WGB are less scattered than that in the SGB. In essence, two issues
305 related to the roughness structures have now come up: the WGB organized (gravels with their
306 longest axis oriented streamwise) and the SGB irregular (randomly poised roughness elements)
307 bed roughness fluctuations having former with higher roughness size than latter. Then, the
308 immediate question arises: how do the roughness structures affect the temporal and spatial
309 velocity fluctuations that are associated with the estimates of different turbulence parameters?
310 There is no doubt that the higher roughness size in the WGB causes to increase the temporal
311 velocity fluctuations. Besides, the organized bed fluctuations in the WGB induce increased
312 spatial velocity fluctuations at a quasi-regular roughness scale. Conversely, the randomly poised
313 roughness elements in the SGB having a shorter roughness size can also induce both the
314 temporal and spatial velocity fluctuations, but at a slightly reduced magnitude relative to the
315 WGB case. The reason for lesser spatial velocity fluctuations in the SGB is associated with
316 manually screeded bed having randomly oriented gravels (Note: it means that the bed roughness
317 elements do not have organized roughness fluctuations). In the succeeding subsections dealing

319 with the turbulence parameters, the effects of the WGB and SBG roughness structures on
 320 temporal and spatial velocity fluctuations (in near-bed flow zone) involved in various turbulence
 321 parameters will be clearly reflected.



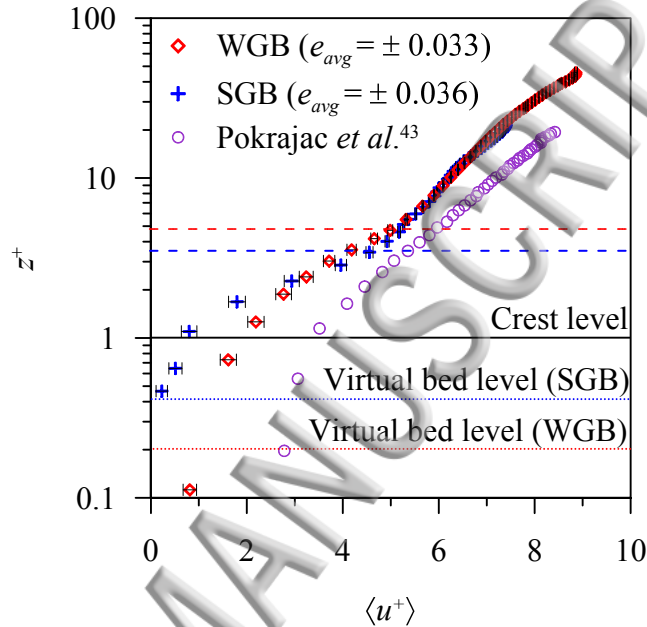
322
 323
 324 FIG. 7. Instantaneous velocity vectors at first measuring section ($x = 6.3$ m) for (a) WGB and (b)
 325 SBG. The vector $\rightarrow 0.25 \text{ m s}^{-1}$ refers to a scale with a magnitude of $(\bar{u}^2 + \bar{w}^2)^{0.5} = 0.25 \text{ m s}^{-1}$.

326
 327 To fit the data plots to a logarithmic law in the flow layer within the end of the wall shear
 328 layer and the crest, the dimensionless DA streamwise velocity $\langle u^+ \rangle$ ($= \langle \bar{u} \rangle / u_*$, where $\langle \bar{u} \rangle$ is the DA
 329 streamwise velocity) and z^+ ($= (z + \Delta z) / \Delta z$, where Δz is the zero-plane displacement) were taken
 330 into consideration. In order to plot the experimental data, the logarithmic law is expressed as

331
 332

$$\langle u^+ \rangle = \frac{1}{\kappa} \ln \left(\frac{z^+}{z_0^+} \right), \quad (2)$$

334 where κ is the von Kármán coefficient ($= 0.41$), $z_0^+ = z_0/\Delta z$, and z_0 is the zero-velocity level. The
 335 values of Δz and z_0 are calculated using the method proposed by Dey and Das⁸ to be 2.21×10^{-3}
 336 and 1.9×10^{-3} m, respectively, for the WGB below the crest. Likewise, the values of Δz and z_0
 337 are 4.81×10^{-3} and 3.59×10^{-3} m, respectively, for the SGB. This indicates that the Δz and z_0 of
 338 the WGB are shallower than those of the SGB.
 339



340
 341
 342 FIG. 8. Variations of the dimensionless DA streamwise velocity $\langle u^+ \rangle$ with the dimensionless
 343 vertical distance z^+ in the WGB, SGB, and Pokrajac *et al.*⁴³ Red and blue dashed lines indicate
 344 the tops of the form-induced WGB and SGB sublayers, respectively.
 345

346 Figure 8 depicts that below the crest, the $\langle u^+ \rangle$ profiles in the WGB and SGB exhibit an
 347 inflection owing to the effects of the roughness geometry function. This result suggests a mixing-
 348 type flow within the interstices of gravels and a momentum sink that appears in the interfacial
 349 sublayer. Owing to interfacial flow within the gravels, the $\langle u^+ \rangle$ profiles are provoked to follow a
 350 third-order polynomial law below the crest ($z^+ \leq 1$).⁸ Importantly, the $\langle u^+ \rangle$ profiles do not follow
 351 the logarithmic law immediately above the crest. Rather they follow a linear law up to the top
 352 edge of the roughness layers ($z^+ = 4.7$ and 3.4 in the WGB and SGB, respectively) owing to the
 353 extended effect of the bed roughness, and thereafter exhibit a logarithmic variation with z , as was
 354 observed by Mignot *et al.*,¹² Sarkar *et al.*⁴⁰ and Pokrajac *et al.*⁴³ Further, to understand the
 355 dispersion of the time-averaged streamwise velocity profiles \bar{u}^+ with respect to the DA
 356 streamwise velocity profile $\langle u^+ \rangle$, the standard error to the mean (SEM) analysis was performed
 357 for both the beds. The dimensionless standard error e ($= \sigma / (n\bar{u}^+)$, where σ is the standard
 358 deviation of \bar{u}^+ profiles with respect to the $\langle u^+ \rangle$ profile, and n is the number of \bar{u}^+ profiles
 359 measured in streamwise direction) was computed and shown in the form of error bars (Fig. 8).
 360 The standard average errors e_{avg} of the $\langle u^+ \rangle$ profiles in the WGB and SGB were ± 0.033 and
 361 ± 0.036 , respectively. The comparison between $\langle u^+ \rangle$ profiles in the WGB and SGB indicates that

362 the $\langle u^+ \rangle$ in the near-bed flow zone of the former is greater than that which occurs in the latter
 363 (Fig. 8). The reason is attributed to the WGB roughness structure. Owing to the water work, the
 364 roughness structure had a tendency to orient the gravels to their longest axis a in the streamwise
 365 direction and intermediate axis b spanwise to them, while that in the SGB was randomly poised.
 366 This makes the near-bed flow to be relatively streamlined in the WGB than in the SGB, although
 367 the roughness in the former is higher than that in the latter. Further, the $\langle u^+ \rangle$ profiles of this study
 368 are compared with that of Pokrajac *et al.*,⁴³ which attains a higher magnitude than those in the
 369 WGB and SGB. The reason is attributed to the geometrically regular roughness size in Pokrajac
 370 *et al.*⁴³ than those in the WGB and SGB.

371 In essence, it is apparent that after a certain distance ($z^+ \geq 3$), the $\langle u^+ \rangle$ profile in the SGB starts
 372 to increase, becoming slightly greater than that in the WGB near the free surface (Fig. 8). This
 373 implies that in the near-bed flow zone, the magnitude of $\langle u^+ \rangle$ in the WGB is greater than that in
 374 the SGB owing to differences in bed surface roughness orientation. However, the effect of the
 375 bed roughness decreases as z^+ increases and one moves toward the free surface.

376 B. SA Reynolds shear stress and form-induced shear stress

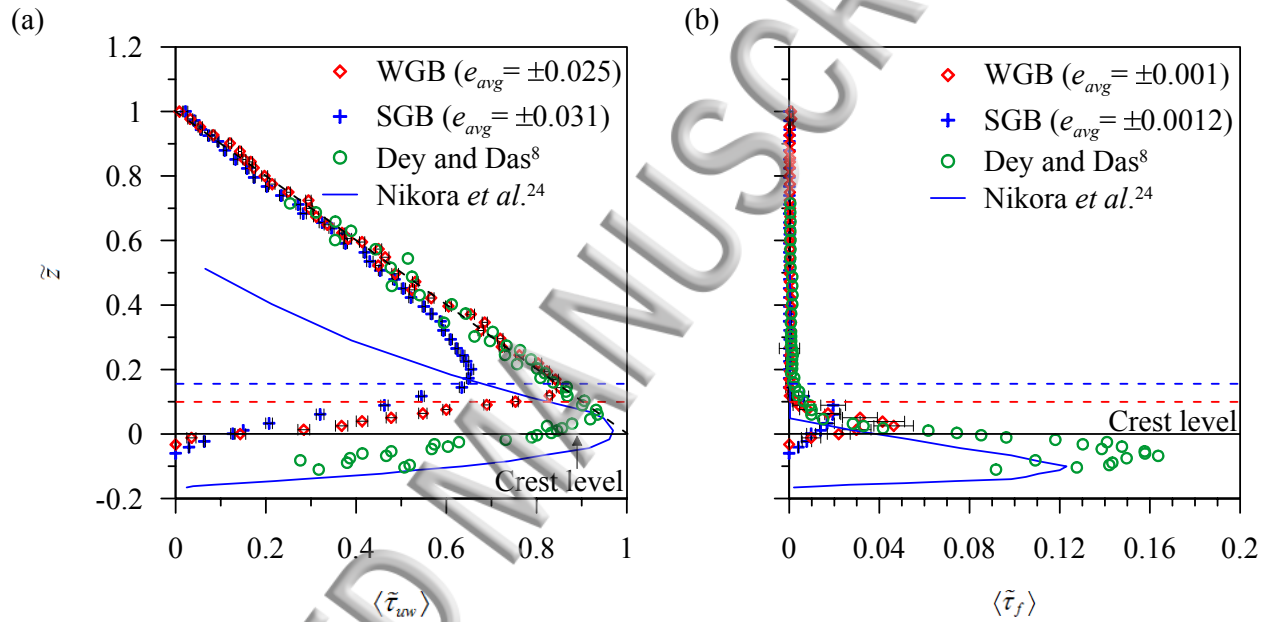
377
 378
 379 For steady, uniform flow over a macro-rough bed, the spatially averaged RANS equations
 380 provide a modified concept of the total fluid shear stress $\langle \bar{\tau} \rangle$.^{8,17,32,44} The $\langle \bar{\tau} \rangle$ is expressed as

$$381 \quad \langle \bar{\tau} \rangle = \langle \tau_f \rangle + \langle \bar{\tau}_{uv} \rangle + \langle \bar{\tau}_v \rangle, \quad (3)$$

382
 383 where $\langle \tau_f \rangle$ is the form-induced shear stress ($= -\rho \langle \tilde{u}\tilde{w} \rangle$), ρ is the mass density of fluid, \tilde{u} and \tilde{w}
 384 are the spatial velocity fluctuations in the streamwise and vertical directions, respectively, $\langle \bar{\tau}_{uv} \rangle$
 385 is the SA RSS ($= -\rho \langle \overline{u'w'} \rangle$), u' and w' are the temporal velocity fluctuations in the streamwise
 386 and vertical directions, respectively, $\langle \bar{\tau}_v \rangle$ is the DA viscous shear stress ($= \rho \nu \langle \bar{u} \rangle / dz$), and ν is
 387 the coefficient of fluid kinematic viscosity. The $\langle \bar{\tau} \rangle$ must be balanced by gravity, and therefore it
 388 has the linear profile $\langle \bar{\tau} (\tilde{z} \geq 1) \rangle \times (\rho u_*^2)^{-1} = 1 - \tilde{z}$. The shear stresses ($\langle \bar{\tau} \rangle$, $\langle \bar{\tau}_{uv} \rangle$, $\langle \tau_f \rangle$, and $\langle \bar{\tau}_v$
 389 \rangle) are made dimensionless by multiplying by $(\rho u_*^2)^{-1}$ and represented as $\langle \tilde{\tau} \rangle$, $\langle \tilde{\tau}_{uv} \rangle$, $\langle \tilde{\tau}_f \rangle$, and \langle
 390 $\tilde{\tau}_v \rangle$.

391
 392 The variations of $\langle \tilde{\tau}_{uv} \rangle$ with \tilde{z} in the WGB and SGB are shown in Fig. 9(a). The peak values
 393 of $\langle \tilde{\tau}_{uv} \rangle$ occur at $\tilde{z} = 0.2$ and 0.27 in the WGB and SGB, respectively, and then decrease as \tilde{z}
 394 increases further. In both the beds, the $\langle \tilde{\tau}_{uv} \rangle$ profiles follow the linear law (linear gravity line)
 395 with \tilde{z} after reaching their peaks. The $\langle \tilde{\tau}_{uv} \rangle$ values start to decrease from $\tilde{z} = 0.15$ and 0.2 in
 396 the WGB and SGB, respectively, as \tilde{z} decreases. However, for $\tilde{z} < 0.14$, the rate of decrease of
 397 $\langle \tilde{\tau}_{uv} \rangle$ becomes faster in the SGB than in the WGB. Damping of $\langle \tilde{\tau}_{uv} \rangle$ in the near-bed flow zone
 398 occurs owing to decreased temporal velocity fluctuations.^{8,12,33,40,45} The results obtained in this
 399 study are compared with those in Dey and Das⁸ and Nikora *et al.*²⁴ It shows that the all the $\langle \tilde{\tau}_{uv} \rangle$
 400 profiles follow the similar trend, except that of Nikora *et al.*²⁴ The $\langle \tilde{\tau}_{uv} \rangle$ profiles depart from the
 401 linear gravity line and dampen within the respective form-induced and interfacial sublayers,

402 resulting from the effects of near-bed flow heterogeneity. Further, the comparison illustrates that
 403 in the near-bed flow zone, a higher roughness in the WGB induces a greater value of $\langle \tilde{\tau}_{inv} \rangle$ than
 404 that in the SGB that possessed a smaller roughness. According to Nezu and Nakagawa,⁴⁶
 405 temporal velocity fluctuations (u' and w') are highly influenced by the bed roughness. To be
 406 explicit, in this study, the bed roughness of the WGB is higher than that of the SGB, giving rise
 407 to higher u' and w' and resulting in greater $\langle \tilde{\tau}_{inv} \rangle$ values in the former than in the latter. This result
 408 is in conformity with the findings of Dey and Das⁸ and Nikora *et al.*²⁴ Further, for the RSS
 409 profiles in both the beds, the standard errors were computed and made dimensionless by dividing
 410 u_*^2 . The average standard errors e_{avg} for the WGB and SGB were computed as ± 0.025 and
 411 ± 0.031 , respectively.
 412



413
 414
 415 FIG. 9. Variations of the dimensionless (a) SA RSS $\langle \tilde{\tau}_{inv} \rangle$ and (b) form-induced shear stress $\langle \tilde{\tau}_f \rangle$
 416 with the dimensionless vertical distance \tilde{z} in the WGB and SGB. The results obtained in this
 417 study are compared with those in Dey and Das⁸ and Nikora *et al.*²⁴
 418

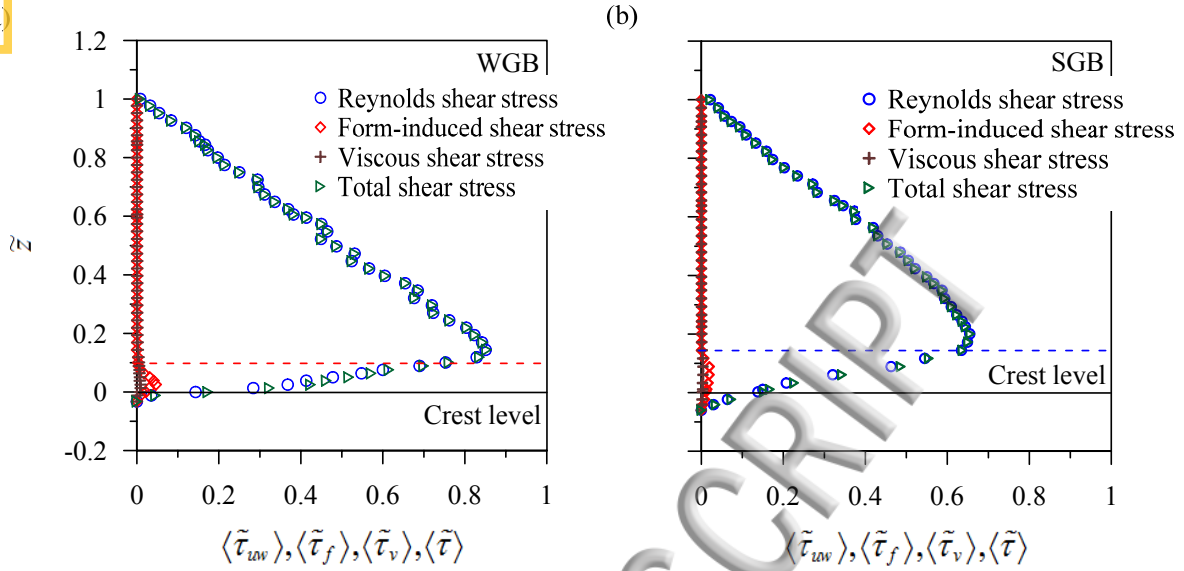
419 Figure 9(b) presents the variations of $\langle \tilde{\tau}_f \rangle$ with \tilde{z} in the WGB and SGB. The $\langle \tilde{\tau}_f \rangle$ starts to
 420 develop at $\tilde{z} = 0.1$ and 0.14 in the WGB and SGB, respectively. This level, which represents the
 421 lower extremity of the wall shear layer, is considered to be the threshold of form-induced
 422 sublayer development.^{8,25} Hence, this criterion is used to determine that the thicknesses of the
 423 form-induced sublayers in the WGB and SGB are $0.1h$ and $0.14h$, respectively. Within the form-
 424 induced sublayer, the $\langle \tilde{\tau}_f \rangle$ profiles grow gradually as \tilde{z} decreases. In the WGB, the magnitude
 425 of $\langle \tilde{\tau}_f \rangle$ attains its peak close to the crest ($\tilde{z} = 0.025$), while in the SGB, the peak appears in the
 426 upper portion of the form-induced sublayer ($\tilde{z} = 0.09$). Thereafter, the values associated with
 427 both the beds start to decline as \tilde{z} decreases. The magnitudes of spatial velocity fluctuations (\tilde{u}
 428 and \tilde{w}) are responsible for this trend in $\langle \tilde{\tau}_f \rangle$. Within the form-induced sublayer, large \tilde{u} and

429 w' values give rise to higher $\langle \tilde{\tau}_f \rangle$ values. Below the crest ($\tilde{z} < 0$), these values are small and
430 thus $\langle \tilde{\tau}_f \rangle$ reduces significantly.^{8,12,32,40,47} The standard errors of the $\langle \tilde{\tau}_f \rangle$ profiles in the near-bed
431 flow zone are larger than those above the roughness layer, where they are negligible for both the
432 beds. Like the RSS profiles, the standard errors of $\langle \tilde{\tau}_f \rangle$ profiles were computed and made
433 dimensionless by dividing u_*^2 . The average standard errors e_{avg} are ± 0.001 and ± 0.0012 for the
434 WGB and SGB, respectively. Further, owing to the spatial variability of roughness elements over
435 entire test section, variations in the spatial velocity fluctuations are relatively high than the
436 temporal velocity fluctuations. Therefore, in this study, the error bars associated with the \tilde{u} and
437 \tilde{w} in Fig 9(b) are to some extent larger than those associated with the u' and w' in Fig. 9(a).

438 For the comparison, the $\langle \tilde{\tau}_f \rangle$ profiles of Dey and Das⁸ and Nikora *et al.*²⁴ are also shown in
439 Fig. 9(b). The comparison corroborates that they follow similar trends, but with different
440 magnitudes. According to Dey and Das⁸ and Sarkar *et al.*,⁴⁰ higher bed surface roughness
441 produces large \tilde{u} and \tilde{w} values, yielding an increased magnitude of $\langle \tilde{\tau}_f \rangle$. In this study, the bed
442 roughness in the WGB is higher than that in the SGB, but smaller than those in Dey and Das⁸
443 and Nikora *et al.*²⁴ As a result, the $\langle \tilde{\tau}_f \rangle$ in the WGB attains a higher value than that in the SGB,
444 but remains smaller than $\langle \tilde{\tau}_f \rangle$ and $\langle \tilde{\tau}_f \rangle$ in Dey and Das⁸ and Nikora *et al.*²⁴, respectively. This
445 indicates that in the near-bed flow zone, the flow is more heterogeneous in the WGB than in the
446 SGB.

447 The variations of $\langle \tilde{\tau}_{uv} \rangle$, $\langle \tilde{\tau}_f \rangle$, $\langle \tilde{\tau}_v \rangle$, and $\langle \tilde{\tau} \rangle$ with \tilde{z} in the WGB and SGB are presented in
448 Figs. 10(a) and 10(b). In both the beds, the $\langle \tilde{\tau}_{uv} \rangle$ profiles dominate throughout the flow depth,
449 except in close proximity to the bed. In the near-bed flow zone ($\tilde{z} < 0.2$), the time-averaged
450 flow becomes spatially heterogeneous, leading to a decrease in $\langle \tilde{\tau}_{uv} \rangle$, although the reduction in \langle
451 $\tilde{\tau}_{uv} \rangle$ is compensated for by $\langle \tilde{\tau}_f \rangle$ and $\langle \tilde{\tau}_v \rangle$. As a result, the $\langle \tilde{\tau} \rangle$ profiles depart from the linear
452 gravity profile. This is resulted from the form-induced fluctuations owing to the influence of the
453 local flow heterogeneity. Moreover, in the near-bed zone, besides the form-induced fluctuations,
454 a form-drag-induced stress is also prevalent.²⁴ However, little progress has so far been made to
455 estimate the form-drag-induced stress, because its precise estimation can only be obtained from
456 the integration of the pressure distribution across the frontal surface of the gravels.^{8,45} Hence, in
457 this study, the $\langle \tilde{\tau} \rangle$ in both the WGB and SGB are not equaling unity near the crest. Similar
458 observations have also been reported by previous researchers.^{8,12,32,40,41,45} In both the beds, the \langle
459 $\tilde{\tau} \rangle$ profiles follow the linear gravity line above the wall shear layer ($\tilde{z} \geq 0.2$), as is typically
460 observed in a zero-pressure gradient flow, approximately equaling the magnitudes of $\langle \tilde{\tau}_{uv} \rangle$, while
461 the magnitudes of $\langle \tilde{\tau}_f \rangle$ and $\langle \tilde{\tau}_v \rangle$ are negligible. From Figs. 10(a) and 10(b), one notices that the
462 RSS peaks appear well above the form-induced sublayer. This implies that u' and w' reach their
463 maxima at this level owing to an intense turbulent mixing process in the near-bed flow zone.
464 This fits with the observations of Manes *et al.*³² and Ferraro *et al.*⁴¹

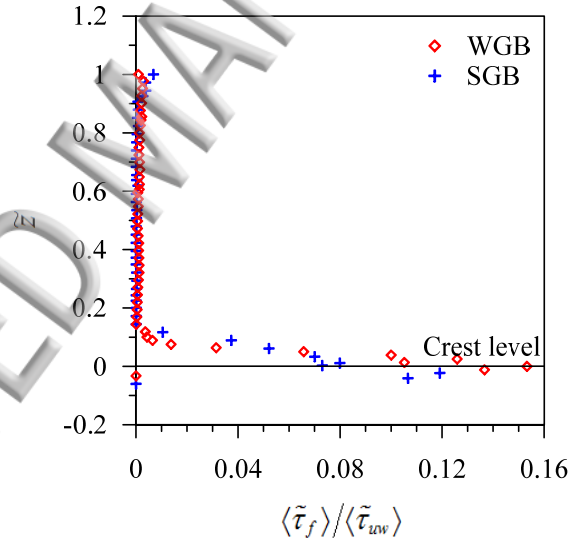
465



466
467

468 FIG. 10. Variations of the dimensionless SA RSS $\langle \tilde{\tau}_{uv} \rangle$, form-induced shear stress $\langle \tilde{\tau}_f \rangle$, DA
469 viscous shear stress $\langle \tilde{\tau}_v \rangle$, and total shear stress $\langle \tilde{\tau} \rangle$ with the dimensionless vertical distance \tilde{z}
470 in (a) the WGB and (b) the SGB.

471



472
473

474 FIG. 11. Variations of the dimensionless form-induced shear stress to SA RSS ratio $\langle \tilde{\tau}_f \rangle / \langle \tilde{\tau}_{uv} \rangle$
475 with the dimensionless vertical distance \tilde{z} in the WGB and SGB.

476

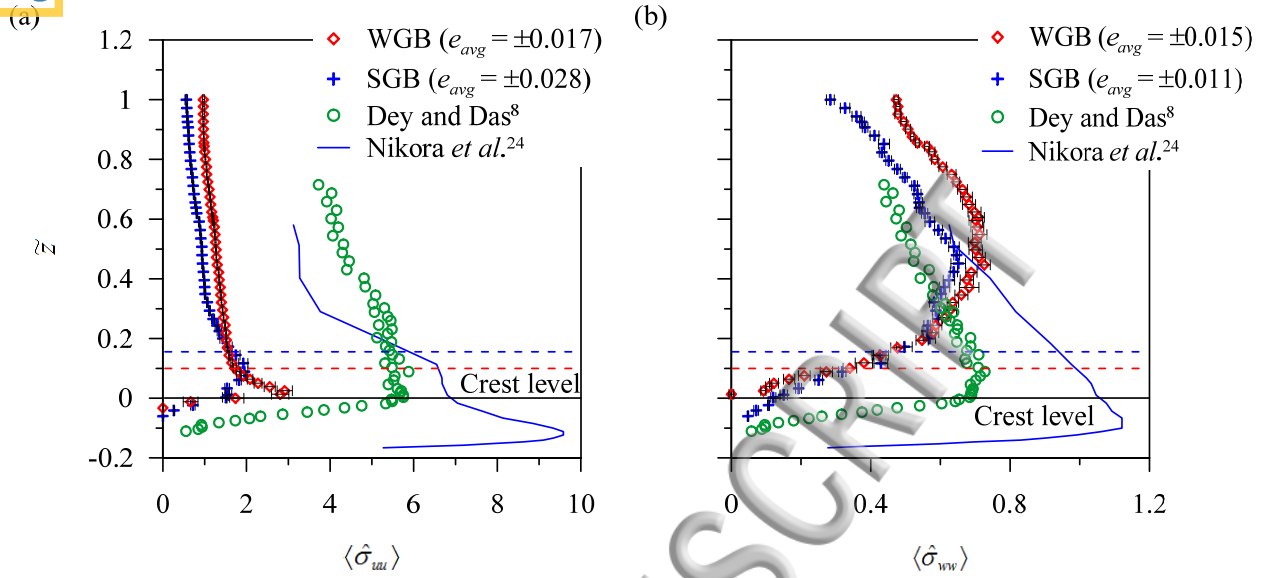
477 Figure 11 illustrates variations of the dimensionless form-induced shear stress to SA RSS ratio
478 $\langle \tilde{\tau}_f \rangle / \langle \tilde{\tau}_{uv} \rangle$ with \tilde{z} in the WGB and SGB. The $\langle \tilde{\tau}_f \rangle / \langle \tilde{\tau}_{uv} \rangle$ profiles start to grow near the top of the
479 roughness layer and then gradually increase as \tilde{z} decreases in both the beds. In the WGB, the \langle
480 $\tilde{\tau}_f \rangle / \langle \tilde{\tau}_{uv} \rangle$ attains its peak at the crest ($\tilde{z} = 0$), while the peak appears just below the crest ($\tilde{z} =$

481 (0.025) in the SGB. Thereafter, they both decrease rapidly with \tilde{z} . The reduction in $\langle \tilde{\tau}_f \rangle / \langle \tilde{\tau}_{uv} \rangle$
 482 within the interfacial sublayer ($\tilde{z} < 0$) is associated with the reduction in $\langle \tilde{\tau}_f \rangle$ relative to $\langle \tilde{\tau}_{uv}$
 483 \rangle .^{8,40} Comparing the $\langle \tilde{\tau}_f \rangle / \langle \tilde{\tau}_{uv} \rangle$ profiles in the WGB and SGB, it indicates that the former is
 484 greater than the latter. According to Dey and Das,⁸ the magnitude of peak of $\langle \tilde{\tau}_f \rangle / \langle \tilde{\tau}_{uv} \rangle$ depends
 485 on the roughness size. The peak of $\langle \tilde{\tau}_f \rangle / \langle \tilde{\tau}_{uv} \rangle$ is larger at higher roughness sizes than at lower
 486 ones. In this study, the bed surface roughness of the WGB is larger than that of the SGB,
 487 producing a larger peak $\langle \tilde{\tau}_f \rangle / \langle \tilde{\tau}_{uv} \rangle$ in the former than in the latter.

488 489 **C. SA Reynolds and form-induced normal stresses** 490

491 The streamwise and vertical SA Reynolds normal stresses are expressed as $\langle \sigma_{uu} \rangle = \rho \langle \overline{u'u'} \rangle$
 492 and $\langle \sigma_{ww} \rangle = \rho \langle \overline{w'w'} \rangle$, respectively, and made dimensionless as $(\langle \hat{\sigma}_{uu} \rangle, \langle \hat{\sigma}_{ww} \rangle) = (\langle \sigma_{uu} \rangle, \langle \sigma_{ww} \rangle) \times$
 493 $(\rho u_*^2)^{-1}$. The dimensionless form-induced normal stresses are expressed in a similar manner as $(\langle$
 494 $\tilde{\sigma}_{uu} \rangle, \langle \tilde{\sigma}_{ww} \rangle) = \rho (\langle \tilde{u}\tilde{u} \rangle, \langle \tilde{w}\tilde{w} \rangle) \times (\rho u_*^2)^{-1}$ in the streamwise and vertical directions, respectively.
 495 The behavior of the dimensionless SA streamwise Reynolds normal stress $\langle \hat{\sigma}_{uu} \rangle$ with respect to
 496 \tilde{z} in the WGB and SGB is shown in Fig. 12(a). In both the beds, the $\langle \hat{\sigma}_{uu} \rangle$ increases with \tilde{z}
 497 within the form-induced sublayer attaining a peak value above the crest. The peak of $\langle \hat{\sigma}_{uu} \rangle \approx$
 498 2.91 in the WGB occurs just above the crest ($\tilde{z} = 0.025$), whereas the peak of $\langle \hat{\sigma}_{uu} \rangle \approx 1.95$ in
 499 the SGB occurs near the top of the form-induced sublayer ($\tilde{z} = 0.09$). In both the cases, the \langle
 500 $\hat{\sigma}_{uu} \rangle$ decreases with further increases in \tilde{z} . According to Dey and Das,⁸ Sarkar *et al.*,⁴⁰ and
 501 Ferraro *et al.*,⁴¹ intense fluid mixing that occurs in the presence of bed roughness is to increase \langle
 502 $\hat{\sigma}_{uu} \rangle$ in the form-induced sublayer. However, the $\langle \hat{\sigma}_{uu} \rangle$ reduces within the interfacial sublayer
 503 owing to damping of the fluid mixing intensity.^{8,40,41}

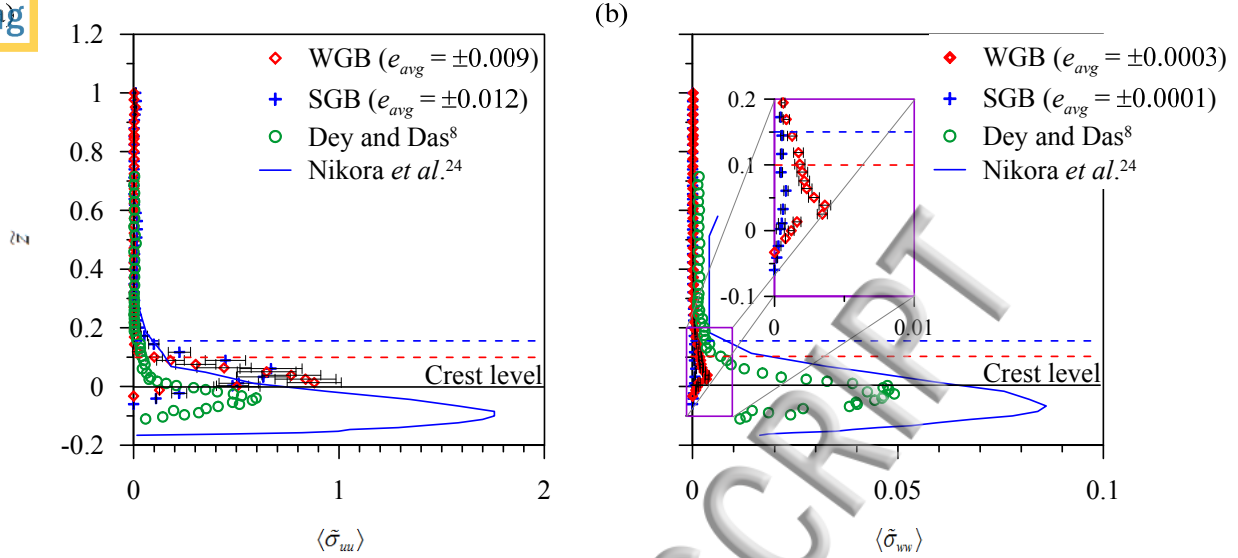
504 A consistency in the trends is found when the $\langle \hat{\sigma}_{uu} \rangle$ profiles of this study are compared with
 505 those of Dey and Das⁸ and Nikora *et al.*²⁴ (Fig. 12(a)). The $\langle \hat{\sigma}_{uu} \rangle$ profiles attain their peaks near
 506 the crest for all the cases, except that for Nikora *et al.*²⁴ The possible reason is attributed to the
 507 loosely packed gravels in Nikora *et al.*²⁴ A close examination of Fig. 12(a) suggests that the main
 508 discrepancy in these profiles lies in the magnitudes of $\langle \hat{\sigma}_{uu} \rangle$. For a given \tilde{z} , the $\langle \hat{\sigma}_{uu} \rangle$ in the
 509 WGB has a greater magnitude than that in the SGB, implying that the WGB exhibits a greater u'
 510 fluctuations than the SGB. However, the magnitudes of $\langle \hat{\sigma}_{uu} \rangle$ in the WGB remain smaller than
 511 those in Dey and Das⁸ and Nikora *et al.*²⁴ owing to greater u' in the latter two cases than the
 512 former. According to Nezu and Nakagawa,⁴⁶ u' is directly associated with the bed roughness. To
 513 be precise, in this study, the higher bed roughness associated with the WGB causes its u'
 514 fluctuations to be enhanced, increasing the magnitude of $\langle \hat{\sigma}_{uu} \rangle$ in the WGB relative to that in the
 515 SGB. The $\langle \hat{\sigma}_{uu} \rangle$ profiles have average standard errors e_{avg} of ± 0.017 for the WGB and ± 0.028
 516 for the SGB.



518
519

520 FIG. 12. Variations of the dimensionless SA (a) streamwise $\langle \hat{\sigma}_{uu} \rangle$ and (b) vertical Reynolds
521 normal stress $\langle \hat{\sigma}_{ww} \rangle$ with dimensionless vertical distance \tilde{z} in the WGB and SGB. The results
522 obtained in this study are compared with those in Dey and Das⁸ and Nikora *et al.*²⁴
523

524 Figure 12(b) shows how the dimensionless SA vertical Reynolds normal stress $\langle \hat{\sigma}_{ww} \rangle$ varies
525 with \tilde{z} in the WGB and SGB. In the WGB, the $\langle \hat{\sigma}_{ww} \rangle$ reaches its peak ($\langle \hat{\sigma}_{ww} \rangle \approx 0.58$) at $\tilde{z} =$
526 0.37 , whereas in the SGB, the peak ($\langle \hat{\sigma}_{ww} \rangle \approx 0.75$) appears at $\tilde{z} = 0.44$. Thereafter, the
527 magnitudes of $\langle \hat{\sigma}_{ww} \rangle$ decrease gradually as \tilde{z} increases in both the beds. This suggests that
528 above the crest, fluid mixing is induced by bed roughness, which enhances w' fluctuations.^{8,41}
529 However, the effects of mixing on w' within the interfacial sublayer are weaker than those above
530 the crest resulting in a lower $\langle \hat{\sigma}_{ww} \rangle$. The $\langle \hat{\sigma}_{ww} \rangle$ profiles of Dey and Das⁸ and Nikora *et al.*²⁴ are
531 also shown in Fig. 12(b) for the comparison with those obtained in this study. Similar to Fig.
532 12(a), the peak values in $\langle \hat{\sigma}_{ww} \rangle$ profiles for three cases occur above the crest, whereas for Nikora
533 *et al.*,²⁴ it is found to be below the crest. The reason is same as stated earlier. It is evident from
534 Fig. 12(b) that the $\langle \hat{\sigma}_{ww} \rangle$ profile in the WGB achieves a higher magnitude than that in the SGB.
535 It implies that the higher bed roughness associated with the WGB, relative to the SGB, induces
536 to increase the w' fluctuations and in turn, the magnitude of $\langle \hat{\sigma}_{ww} \rangle$ is enhanced in the WGB. This
537 phenomenon corresponds to the findings of Dey and Das,⁸ Nikora *et al.*²⁴ and Sarkar *et al.*⁴⁰ The
538 average standard errors e_{avg} in $\langle \hat{\sigma}_{ww} \rangle$ profiles calculated for the WGB and SGB are ± 0.015 and
539 ± 0.011 , respectively.
540



541
542

543 FIG. 13. Variations of the dimensionless (a) streamwise $\langle \tilde{\sigma}_{uu} \rangle$ and (b) vertical form-induced
544 normal stress $\langle \tilde{\sigma}_{vv} \rangle$ with the dimensionless vertical distance \tilde{z} in the WGB and SGB. The
545 results obtained in this study are compared with those in Dey and Das⁸ and Nikora *et al.*²⁴
546

547 The behaviors of the dimensionless streamwise form-induced normal stress $\langle \tilde{\sigma}_{uu} \rangle$ in the
548 WGB and SGB are presented in Fig. 13(a). In both the beds, the $\langle \tilde{\sigma}_{uu} \rangle$ profiles grow as \tilde{z}
549 decreases, starting from $\tilde{z} = 0.1$ and $\tilde{z} = 0.14$, respectively. In the WGB, the peak of $\langle \tilde{\sigma}_{uu} \rangle$
550 exists just above the crest ($\tilde{z} = 0.01$), whereas in the SGB, the peak occurs near the middle of
551 the form-induced sublayer ($\tilde{z} = 0.06$). However, the $\langle \tilde{\sigma}_{uu} \rangle$ decreases with a further decrease in
552 \tilde{z} in both the beds. This suggests that within the form-induced sublayer, the $\langle \tilde{\sigma}_{uu} \rangle$ increases
553 owing to increased spatial velocity fluctuations \tilde{u} , whereas within the interfacial sublayer, the
554 $\langle \tilde{\sigma}_{uu} \rangle$ decreases with \tilde{u} . Above the form-induced sublayer, the $\langle \tilde{\sigma}_{uu} \rangle$ is almost negligible in both
555 the beds. The average standard errors e_{avg} of the $\langle \tilde{\sigma}_{uu} \rangle$ profiles are of ± 0.009 and ± 0.012 for the
556 WGB and SGB, respectively. Figure 13(a) demonstrates that the $\langle \tilde{\sigma}_{uu} \rangle$ in the WGB is greater
557 than that in the SGB owing to the higher \tilde{u} in the former. However, the WGB $\langle \tilde{\sigma}_{uu} \rangle$ is found to
558 be less when it is compared with that of Nikora *et al.*²⁴ This confirms that \tilde{u} are directly
559 associated with the roughness size. The $\langle \tilde{\sigma}_{uu} \rangle$ profiles of Dey and Das⁸ are slightly smaller in
560 magnitude than those obtained in the WGB. The roughness structure formed by the gravels in the
561 WGB was well organized (as discussed in section IIIA), whereas in Dey and Das,⁸ the roughness
562 structure was randomly poised. This may result in smaller values of $\langle \tilde{\sigma}_{uu} \rangle$ in Dey and Das⁸ than
563 those in the WGB.

564 Figure 13(b) shows the dimensionless vertical form-induced normal stress $\langle \tilde{\sigma}_{vv} \rangle$ variations in
565 the WGB and SGB. Further, in order to have an enlarged view, the $\langle \tilde{\sigma}_{vv} \rangle$ profiles in the near-bed

566 flow zone are shown in inset in Fig. 13(b). As with the $\langle \tilde{\sigma}_{uu} \rangle$ profiles, the $\langle \tilde{\sigma}_{ww} \rangle$ profiles reflect
 567 similar trends in both the beds. The $\langle \tilde{\sigma}_{ww} \rangle$ profiles in the WGB and SGB reach their peaks at \tilde{z}
 568 $= 0.025$ and 0.075 , respectively. For $\tilde{z} < 0$, the $\langle \tilde{\sigma}_{ww} \rangle$ decreases significantly with \tilde{z} . The
 569 magnitude of $\langle \tilde{\sigma}_{ww} \rangle$ depends on the variations in the spatial velocity fluctuations \tilde{w} .^{8,12,40,41,48}
 570 The comparative study suggests that the $\langle \tilde{\sigma}_{ww} \rangle$ values in both Dey and Das⁸ and Nikora *et al.*²⁴
 571 are much larger than those obtained in this study. This occurs as a result of much higher
 572 roughness elements used in Dey and Das⁸ and Nikora *et al.*²⁴ than those in the WGB and SGB,
 573 because higher roughness induces greater \tilde{w} . Reverting to this study, Fig. 13(b) shows that there
 574 exists a difference between the peak values in the WGB and SGB. The possible reason behind
 575 this is their difference in roughness size. In the $\langle \tilde{\sigma}_{ww} \rangle$ profiles, the average standard errors e_{avg}
 576 for the WGB and SGB are of ± 0.0003 and ± 0.0001 , respectively. One can notice that the error
 577 bars associated with $\langle \tilde{\sigma}_{uu} \rangle$ profiles are longer than those with $\langle \tilde{\sigma}_{ww} \rangle$ profiles. The reason is
 578 attributed to the spatial flow variability in the streamwise direction than that in the vertical
 579 direction.

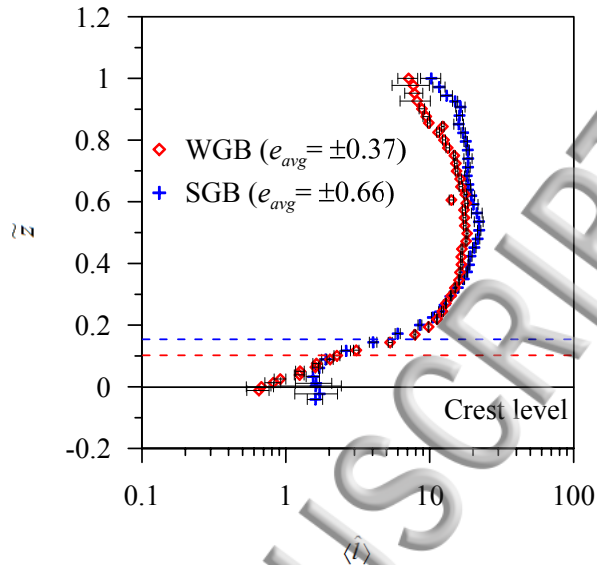
580 D. DA Prandtl mixing length

581 The mixing length concept was introduced first by Prandtl.⁴⁹ The mixing length (l) is defined
 582 as the average length travelled by the fluid parcels from their generation to degeneration to
 583 change their momentum in the ambient fluid. To apply this concept to flow over a macro-rough
 584 bed, one must double-average the Prandtl mixing length. Thus, the DA Prandtl mixing length $\langle l \rangle$
 585 in flow over a gravel bed can be given by
 586
 587
 588

$$589 \quad \langle l \rangle = \frac{(\overline{\langle u'w' \rangle})^{0.5}}{d\langle \bar{u} \rangle / dz}. \quad (4)$$

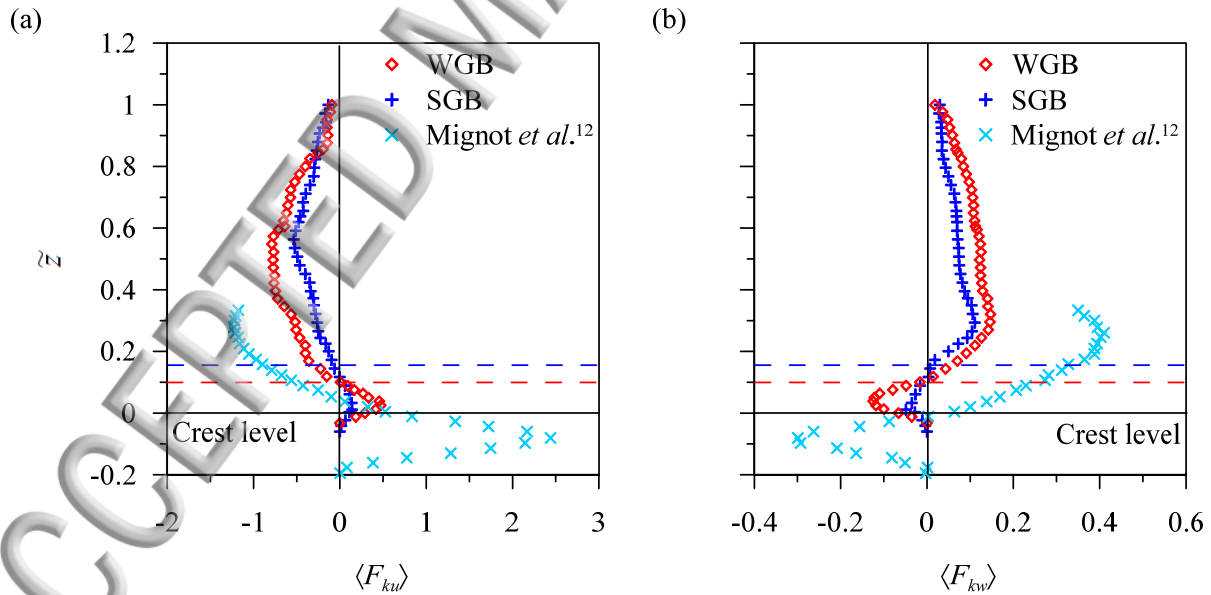
590 The DA Prandtl mixing length $\langle l \rangle$ is expressed in dimensionless form as $\langle \hat{l} \rangle = \langle l \rangle / k_s$. Figure 14
 591 shows how the $\langle \hat{l} \rangle$ varies with \tilde{z} in the WGB and SGB. In the context of existing (traditional)
 592 understanding of l in a hydraulically rough flow, l varies linearly with z within the wall shear
 593 layer ($z \leq 0.2h$).²³ It is however evident that the $\langle \hat{l} \rangle$ in the WGB almost varies linearly with \tilde{z} up
 594 to $z \approx 0.2h$, complying with the traditional variation. On the other hand, in case of the SGB, the \langle
 595 $\hat{l} \rangle$ remains almost invariant with \tilde{z} in the close proximity of the bed up to $z \approx 0.05h$; however, it
 596 varies linearly for $0.05 \geq \tilde{z} \geq 0.2$. Thereafter, the values of $\langle \hat{l} \rangle$ in both the beds grow slowly
 597 becoming almost invariant with \tilde{z} as one moves upward. The possible reason for the departure
 598 of the near-bed $\langle \hat{l} \rangle$ profile in the SGB from that in the WGB is attributed to the effects of
 599 randomly poised roughness structures in the SGB. Owing to the randomly poised roughness
 600 structures in the SGB, the flow velocity decelerates in the near-bed flow zone (as earlier
 601 discussed in section IIIA). In addition, smaller roughness size in the SGB than that in the WGB
 602 is to produce lesser near-bed u' and w' in the SGB than those in the WGB. As a result, in the
 603 near-bed flow zone, the $\langle \hat{l} \rangle$ in the SGB is found to be smaller than that in the WGB. The average
 604

605 standard errors e_{avg} of the $\langle \hat{l} \rangle$ profiles vary within the range of ± 0.37 for the WGB and ± 0.66 for
 606 the SGB.
 607



608
 609
 610 FIG. 14. Variations of the dimensionless DA Prandtl mixing length $\langle \hat{l} \rangle$ with the dimensionless
 611 vertical distance \tilde{z} in the WGB and SGB.
 612

613 **E. SA turbulent kinetic energy and form-induced turbulent kinetic energy fluxes**
 614



615
 616
 617 FIG. 15. Variations of the dimensionless SA (a) streamwise $\langle F_{ku} \rangle$ and (b) vertical TKE flux $\langle F_{kw} \rangle$
 618 with the dimensionless vertical distance \tilde{z} in the WGB and SGB. The results obtained in this
 619 study are compared with those in Mignot *et al.*¹²
 620

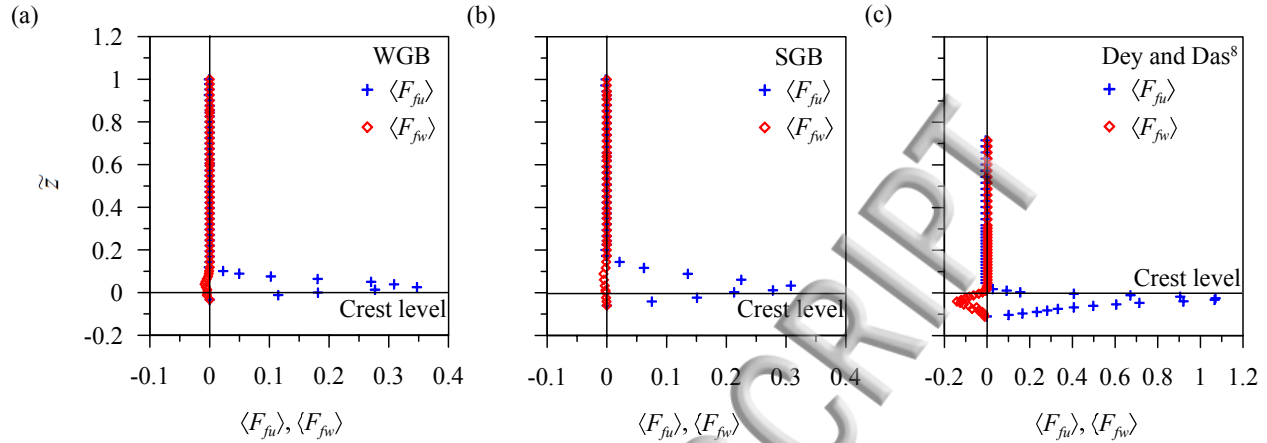
622 The SA TKE fluxes are made dimensionless as $(\langle F_{ku} \rangle, \langle F_{kw} \rangle) = (\langle f_{ku} \rangle, \langle f_{kw} \rangle) \times u_*^{-3}$. Variations
 623 of the dimensionless SA streamwise $\langle F_{ku} \rangle$ and vertical $\langle F_{kw} \rangle$ TKE fluxes with \tilde{z} in the WGB and
 624 SGB are shown in Figs. 15(a) and 15(b), respectively. Since the flow measurement was two-
 625 dimensional, the streamwise and vertical TKE fluxes are therefore estimated using $f_{ku} = 0.75(\frac{u'u'u' + u'w'w'}{u'u'u' + u'w'w'})$ and $f_{kw} = 0.75(\frac{u'u'w' + w'w'w'}{u'u'w' + w'w'w'})$, respectively.²³ In Fig. 15(a), the $\langle F_{ku} \rangle$ in the
 626 WGB starts positive, reaching its peak just above the crest ($\tilde{z} = 0.025$). It then decreases as \tilde{z}
 627 increases further, but remains positive until $\tilde{z} = 0.1$. The $\langle F_{ku} \rangle$ profile in the SGB follows a trend
 628 similar to that in the WGB. The positive peak of $\langle F_{ku} \rangle$ in the SGB appears at $\tilde{z} \approx 0.01$ and the
 629 sign of the $\langle F_{ku} \rangle$ changes after $\tilde{z} = 0.088$. According to Dey and Das,⁸ Mignot *et al.*,¹² and
 630 Sarkar *et al.*,⁴⁰ a positive $\langle F_{ku} \rangle$ value indicates a streamwise transport of the TKE flux, whereas a
 631 negative value suggests an upstream transport of the TKE flux. Figure 15(a) depicts that the $\langle F_{ku} \rangle$
 632 in the WGB is greater than that in the SGB, implying the WGB to have higher u' and w' than the
 633 SGB. However, the $\langle F_{ku} \rangle$ in the WGB remain smaller than that in Mignot *et al.*¹² owing to higher
 634 u' and w' in the latter than that in the former. Moreover, the u' and w' fluctuations are directly
 635 associated with the bed roughness, as discussed earlier. To be explicit, in this study, owing to the
 636 higher roughness in the WGB than that in the SGB, the $\langle F_{ku} \rangle$ is greater in the former than in the
 637 latter.

638 In Fig. 15(b), the $\langle F_{kw} \rangle$ profiles in the WGB and SGB start with small negative values within
 639 the interfacial sublayer and attain their respective negative peaks at $\tilde{z} = 0.025$ and 0. The
 640 absolute magnitude of $\langle F_{kw} \rangle$ then starts to diminish with further increases in \tilde{z} , becoming
 641 positive for $\tilde{z} > 0.1$ and 0.088 in the WGB and SGB, respectively. Negative and positive $\langle F_{kw} \rangle$
 642 values indicate downward and upward transport of vertical flux, respectively.^{8,23,40,45} For the
 643 comparison, the $\langle F_{kw} \rangle$ profile of Mignot *et al.*¹² is shown in Fig. 15(b). The comparative study
 644 suggests that for a given \tilde{z} , the magnitude of $\langle F_{kw} \rangle$ follows a sequence of $\langle F_{kw} \rangle$ in Mignot *et al.*¹²
 645 $> \langle F_{kw} \rangle$ in the WGB $> \langle F_{kw} \rangle$ in the SGB. The reason for such sequence is attributed to descending
 646 sizes of roughness, as described earlier in reference to the $\langle F_{ku} \rangle$ profiles.

647 According to Dey and Das,⁸ Sarkar *et al.*,⁴⁰ and Sarkar and Dey,⁴⁵ the streamwise and vertical
 648 TKE flux profiles provide information about the bursting events. The combination of a positive
 649 $\langle F_{ku} \rangle$ and a negative $\langle F_{kw} \rangle$ gives rise to sweep or Q_4 events (that is, the inrush of fluid parcels).
 650 Conversely, the combination of a negative $\langle F_{ku} \rangle$ and a positive $\langle F_{kw} \rangle$ gives rise to ejection or Q_2
 651 events (that is, the arrival of slowly moving fluid parcels). In this study, the sweep events are
 652 dominant up to $\tilde{z} = 0.1$ and 0.088 in the WGB and SGB, respectively (Fig. 15(a)). In contrast,
 653 the ejection events are dominant at $\tilde{z} > 0.1$ and 0.088 in the WGB and SGB, respectively (Fig.
 654 15(b)).

655 The dimensionless streamwise and vertical form-induced TKE fluxes are obtained using
 656 $(\langle F_{fu} \rangle, \langle F_{fv} \rangle) = (\langle f_{fu} \rangle, \langle f_{fv} \rangle) \times u_*^{-3}$, respectively, where $\langle f_{fu} \rangle$ is the streamwise form-induced TKE
 657 flux expressed as $0.75(\langle \tilde{u}\tilde{u}\tilde{u} \rangle + \langle \tilde{u}\tilde{w}\tilde{w} \rangle)$ and $\langle f_{fv} \rangle$ is the vertical form-induced TKE flux expressed
 658 as $0.75(\langle \tilde{u}\tilde{u}\tilde{w} \rangle + \langle \tilde{w}\tilde{w}\tilde{w} \rangle)$. The behaviors of $\langle F_{fu} \rangle$ and $\langle F_{fv} \rangle$ with respect to \tilde{z} in the WGB and
 659 SGB are shown in Figs. 16(a) and 16(b), respectively. In both the beds, the $\langle F_{fu} \rangle$ starts with
 660 positive values within the interfacial sublayer and increases gradually with \tilde{z} . In the WGB, the
 661 $\langle F_{fu} \rangle$ reaches its positive peak above the crest ($\tilde{z} = 0.025$), whereas the peak appears at $\tilde{z} = 0.01$
 662 in the SGB. Thereafter, both values tend to decrease with \tilde{z} . In both the beds, the $\langle F_{fu} \rangle$ nearly
 663 vanishes above the form-induced sublayer. The \tilde{u} fluctuations in the WGB are higher than those

664 ing the SGB, as evident from Fig. 13(a)), resulting in higher $\langle F_{fu} \rangle$ in the former than in the latter at
 665 a given \tilde{z} .
 666



667
 668
 669 FIG. 16. Variations of the dimensionless streamwise form-induced TKE flux $\langle F_{fu} \rangle$ and vertical
 670 form-induced TKE flux $\langle F_{fw} \rangle$ with the dimensionless vertical distance \tilde{z} in (a) the WGB, (b) the
 671 SGB, and (c) Dey and Das⁸.
 672

673 In both the beds, the $\langle F_{fw} \rangle$ profiles that are negative start to grow within the interfacial
 674 sublayer as \tilde{z} increases (Figs. 16(a) and 16(b)). The $\langle F_{fw} \rangle$ profiles reach their respective negative
 675 peaks at $\tilde{z} \approx 0.039$ and 0.06 in the WGB and SGB, respectively. However, the magnitudes of
 676 $\langle F_{fw} \rangle$ gradually decrease after achieving their negative peaks as one moves toward the top edge of
 677 the form-induced sublayer, and thereafter become negligible. One can argue that \tilde{w} is
 678 significantly weaker than \tilde{u} , resulting in a $\langle F_{fw} \rangle$ that is smaller than a $\langle F_{fu} \rangle$ at a given \tilde{z} .
 679 Comparison of Figs. 16(a)–16(c) shows that the magnitudes of form-induced TKE fluxes in the
 680 WGB are greater than those in the SGB, whereas they remain smaller than those in Dey and Das⁸
 681 in the near-bed flow zone. This can be interpreted as the effects of the difference in bed
 682 roughness in the three cases.
 683

684 G. Conditional statistics of Reynolds shear stress

685
 686 Conditional statistical analysis of the RSS provide insight into the dynamics of coherent
 687 structure in turbulent flow.⁵⁰ In this analysis, the temporal velocity fluctuations u' and w' are
 688 decomposed into four quadrants in the $u'w'$ plane. To differentiate stronger and weaker events,
 689 the hole size H and the detection function $\lambda_{i,H}(t)$ are used. The detection function $\lambda_{i,H}(t) = 1$ when
 690 $|u'w'| \geq H (\overline{u'u'})^{0.5} (\overline{w'w'})^{0.5}$. Otherwise $\lambda_{i,H}(t) = 0$. Hence, larger velocity fluctuations (stronger
 691 events) that contribute to the RSS can be identified from each quadrant plot by leaving the
 692 smaller velocity fluctuations (weaker events) within the hole.^{8,25,26} The contributions of bursting
 693 events to the total RSS from quadrant i outside the hole can be obtained from
 694

$$695 \quad \overline{u'w'}_{i,H} = \lim_{T \rightarrow \infty} \frac{1}{T} \int_0^T u'(t)w'(t)\lambda_{i,H}(z,t)dt, \quad (5)$$

696

where T is the sampling time. Depending on the sign convention, the bursting events are characterized. This includes Q_1 events, which are outward interactions ($i = 1, u' > 0$ and $w' > 0$), Q_2 events, which are ejections ($i = 2, u' < 0$ and $w' > 0$), Q_3 events, which are inward interactions ($i = 3, u' < 0$ and $w' < 0$), and Q_4 events, which are sweeps ($i = 4, u' > 0$ and $w' < 0$). The fractional contribution of the conditional RSS ($S_{i,H}$) of each event to the total RSS is represented using

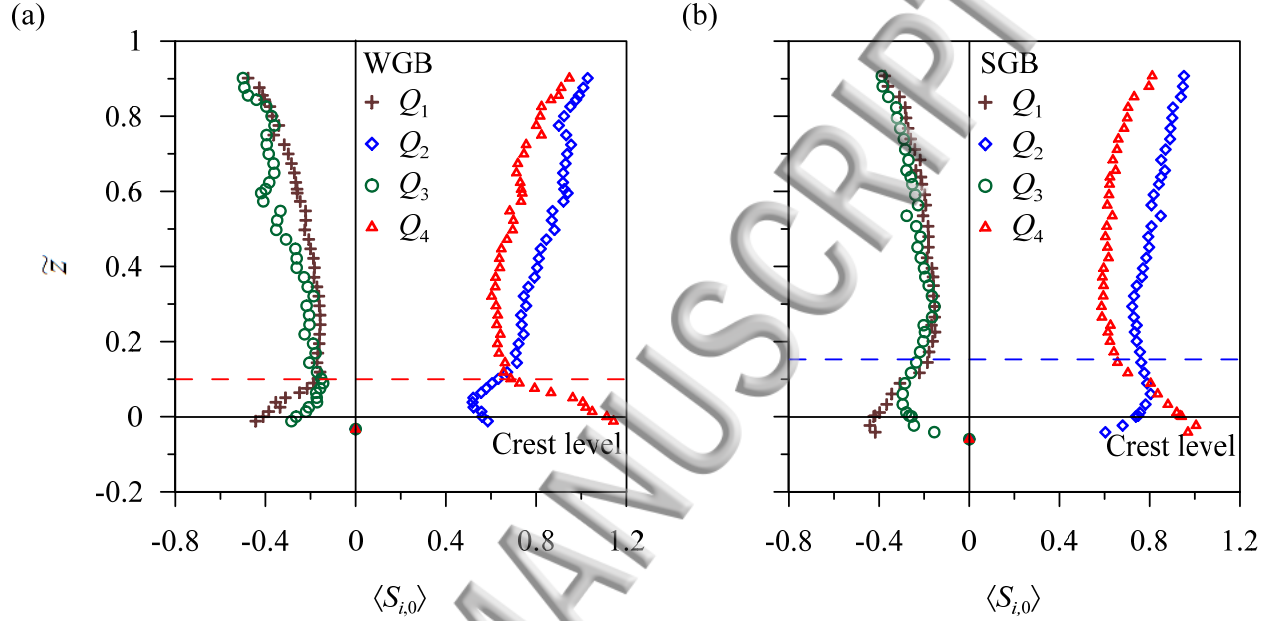


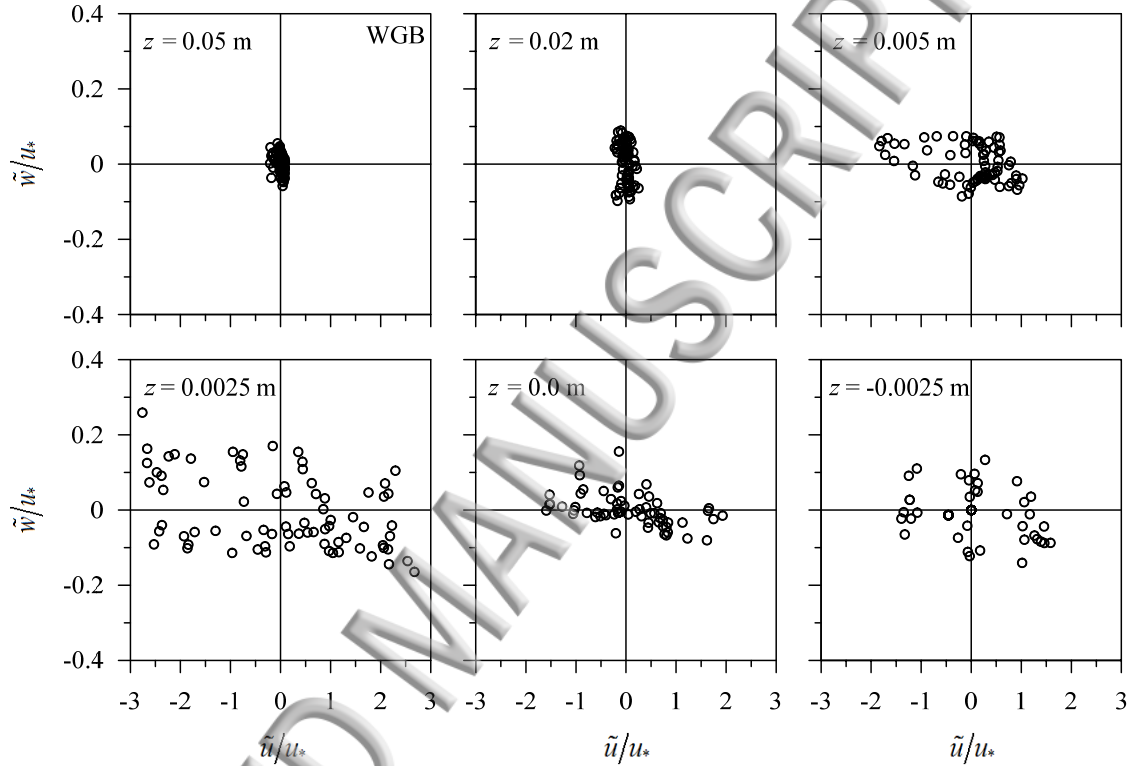
FIG. 17. Variations of the fractional contributions to the conditional SA RSS $\langle S_{i,0} \rangle$ with the dimensionless vertical distance \tilde{z} in (a) the WGB and (b) the SGB.

$$S_{i,H} = \frac{\overline{u'w'_{i,H}}}{\overline{u'w'}}. \quad (6)$$

The variations of the DA fractional contributions $\langle S_{i,H} \rangle$ with \tilde{z} in the WGB and SGB when $H = 0$ are presented in Figs. 17(a) and 17(b), respectively. Although u' and w' have small magnitudes within the interfacial sublayer, they play vital roles in the analysis of turbulence characteristics. Therefore, all plots of u' and w' at $H = 0$ are considered when calculating $\langle S_{i,H} \rangle$.^{8,45}

Figures 17(a) and 17(b) indicate that contributions from the Q_2 events to the total RSS increase with \tilde{z} above the wall shear layer ($\tilde{z} > 0.2$) and continue to be larger than the contributions from Q_4 events up to the free surfaces of both the beds. Contributions from Q_1 and Q_3 events are insignificant when compared to those from Q_2 and Q_4 events, as has been commonly observed in rough-bed flows.^{8,12,40,45} In Fig. 17(a), at the crest ($\tilde{z} = 0$), the contributions from the Q_2 and Q_4 events represent approximately 58% and 110% ($\langle S_{2,0} \rangle \approx 0.58$ and $\langle S_{4,0} \rangle \approx 1.1$), respectively. Conversely, the contributions from Q_1 and Q_3 events at the crest are approximately 22% and 40% ($\langle S_{1,0} \rangle \approx 0.22$ and $\langle S_{3,0} \rangle \approx 0.4$), respectively. When $\tilde{z} > 0$, the contribution from Q_4 events decreases as \tilde{z} increases, while that from Q_2 events increases. The

726 contributions become equal ($\langle S_{2,0} \rangle \approx \langle S_{4,0} \rangle \approx 0.79$) at $\tilde{z} = 0.1$. As \tilde{z} increases further, the
 727 contribution from Q_2 events becomes larger than that from Q_4 events, becoming dominant for the
 728 rest of the vertical distance z . This indicates that sweep or Q_4 events dominate within the
 729 roughness layer ($\tilde{z} = 0.1$). The dominance of sweep events indicates an inrush of faster-moving
 730 fluid parcels within the interfaces of gravels. Hence, sweep events are governed by the flow
 731 within the near-bed flow zone and consequently, the magnitude of SA RSS is diminished in this
 732 flow zone.

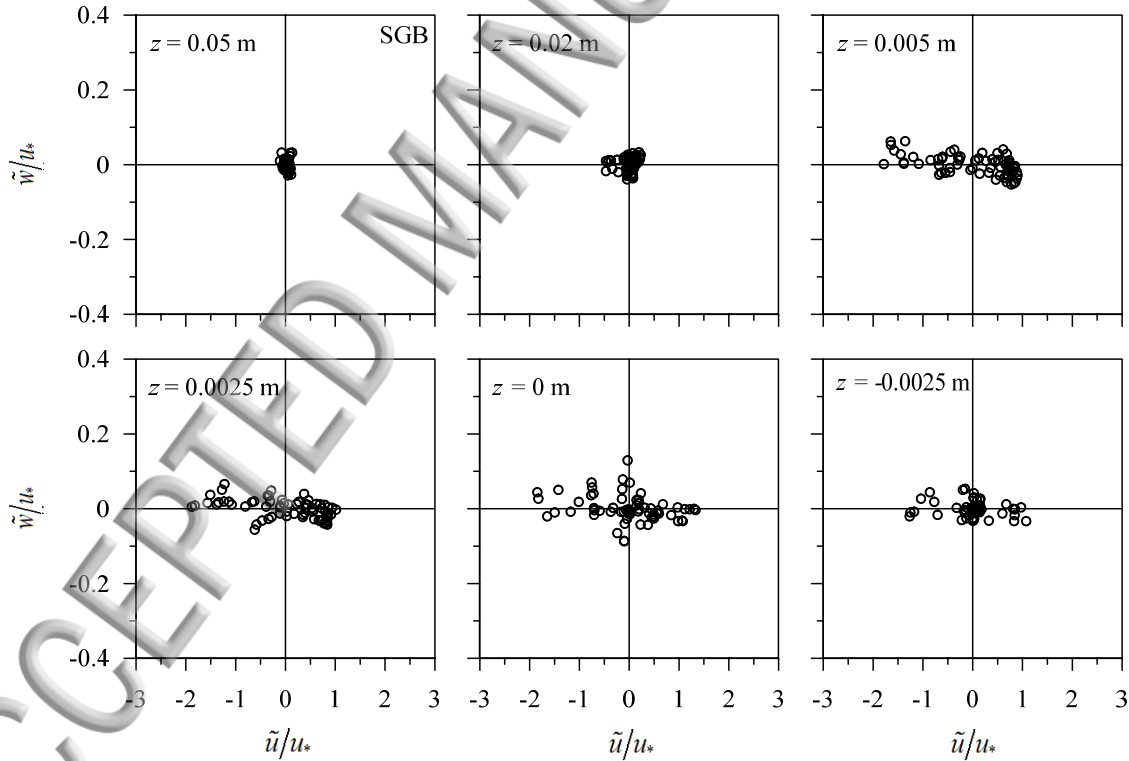


733
 734
 735 FIG. 18. Quadrant plots of spatial velocity fluctuations at different vertical distances z in the
 736 WGB.

737
 738 In the SGB, the profiles of the Q_1 , Q_2 , Q_3 , and Q_4 events follow trends similar to those in the
 739 WGB (Fig. 17(b)). The contribution from Q_4 events equals to that from Q_2 events ($\langle S_{2,0} \rangle \approx \langle S_{4,0} \rangle$
 740 ≈ 0.8) at the middle of the form-induced sublayer ($\tilde{z} = 0.088$). When $\tilde{z} > 0.088$, the
 741 contribution from Q_2 events is greater than that from Q_4 events. From Figs. 17(a) and 17(b), one
 742 can see that the profiles of the Q_2 and Q_4 events in the WGB and SGB are similar except in the
 743 near-bed flow zone. In the WGB, the contribution from Q_4 events reaches its peak at $\tilde{z} = -0.025$
 744 and then begins to decrease as \tilde{z} increases further. Within the interfacial sublayer, the
 745 contribution from the Q_4 events in the SGB increases with \tilde{z} until it reaches its peak just below
 746 the crest, at which point it decreases. The contribution from Q_2 events in the WGB decreases
 747 until $\tilde{z} = 0.05$, but increases with \tilde{z} thereafter. In contrast, the contribution from Q_2 events in
 748 the SGB starts to increase within the interfacial sublayer, maintaining almost same magnitude
 749 throughout the flow depth. In the near-bed flow zone, the fractional contribution to the total RSS

751 from Q_4 events is higher in the WGB than in the SGB. One possible reason is the presence of
 752 higher u' and w' fluctuations in the WGB than in the SGB.

753 A quadrant analysis of the spatial velocity fluctuations, \tilde{u} and \tilde{w} , in the $\tilde{u}\tilde{w}$ domain was
 754 performed for the WGB and SGB.^{40,45} In the quadrant plots, \tilde{u} and \tilde{w} are made dimensionless by
 755 dividing by u^* . The results for the WGB and SGB are shown in Figs. 18 and 19, respectively.
 756 The \tilde{u} and \tilde{w} plots of six different vertical locations are presented at $z = -0.0025$ m (below the
 757 crest), 0 m (at the crest), 0.0025 m, 0.005 m, 0.02 m, and 0.05 m (above the crest). In the WGB,
 758 the $z = 0.005$ m, 0.0025 m, 0, and -0.0025 m plots form a pseudo-elliptical shape with a major
 759 axis inclined toward the x axis. However, for $z = 0.02$ and 0.05 m, the plots form an irregular
 760 elliptical cluster. From Fig. 18, it is apparent that \tilde{u} and \tilde{w} tend to vanish at the outer extremity
 761 and above the wall shear layer ($\tilde{z} \geq 0.2$). However, these values are finite in the near-bed flow
 762 zone. The ellipse is largest at $\tilde{z} = 0.025$. This indicates that the form-induced stress is at its
 763 maximum when $\tilde{z} = 0.025$, decreasing when \tilde{z} either increases or decreases. A similar trend is
 764 observed in the SGB (Fig. 19). Upon comparing Figs. 18 and 19, one finds that the \tilde{u} and \tilde{w} in
 765 the WGB appear to be more scattered and have higher magnitudes than those in the SGB. This
 766 implies that water work causes significant changes in gravel orientation, as well as in the bed
 767 surface roughness, resulting in higher spatial velocity fluctuations in the WGB than in the SGB.
 768



769
 770
 771 FIG. 19. Quadrant plots of spatial velocity fluctuations at different vertical distances z in the
 772 SGB.

773
 774 **IV CONCLUDING REMARKS**
 775

777 The turbulence characteristics of flows over a WGB and an SGB were measured using a two-
778 dimensional particle image velocimetry and analyzed by applying the DAM. Although the flow
779 conditions in both the beds were identical, significant differences in the velocity and turbulence
780 characteristics were noted, especially in the near-bed flow zone. This was induced by the
781 differences between the WGB and SGB roughness structures that were composed of different
782 orientations of surface gravels. Importantly, owing to the action of water work, the longest axis
783 of WGB gravels were oriented streamwise, while SGB gravels were randomly poised. The DA
784 streamwise velocity profiles in both the beds follow the logarithmic law above the form-induced
785 sublayer, but follow linear and third-order polynomial laws within the form-induced and
786 interfacial sublayers, respectively. Although the DA streamwise velocity profiles follow similar
787 trend in the WGB and SGB, the near-bed velocity profile in the former is greater than that in the
788 latter. It is resulted from the near-bed flow to be relatively streamlined in the WGB (in which the
789 longest axis of gravels were systematically oriented streamwise) than in the SGB (in which the
790 gravels were randomly poised), although the roughness in the former is higher than that in the
latter.

791 In both the beds, the SA RSS profiles reach their peaks above the wall shear layer, continuing
792 to decrease toward the free surface and closely following the linear law (linear gravity line) with
793 vertical distance. In the near-bed flow zone, the SA RSS is larger in the WGB than in the SGB
794 owing to the presence of larger temporal velocity fluctuations in the former. Within the
795 roughness layer, the form-induced shear stress values in both the beds reach their peaks above
796 the crest, and thereafter decrease toward the outer edge of the form-induced sublayer. Owing to
797 greater spatial velocity fluctuations in the WGB, the form-induced shear stress in the WGB is
798 greater than that in the SGB. The SA Reynolds normal stress components are small in the near-
799 bed flow zone and grow as the vertical distance increases in both the WGB and SGB. They reach
800 their peaks above the crest. As a result of higher temporal velocity fluctuations in the WGB, its
801 SA Reynolds normal stress components are larger than those in the SGB.

802 Analysis shows that the DA Prandtl mixing lengths in the WGB and SGB are small within the
803 interfacial sublayer. However, they increase above the form-induced sublayer. The SA TKE
804 fluxes in the WGB are small in the near-bed flow zone and change their signs above the crest.
805 Although similar trends appear in the SGB, significant differences between the magnitudes of the
806 SA TKE fluxes in the WGB and SGB are observed in the near-bed flow zone.

807 A quadrant analysis of temporal velocity fluctuations confirms that sweep events dominate in
808 the near-bed flow zone, and that the character of this dominance changes above the crests of both
809 the beds. Sweep events tend to dominate more in the WGB than in the SGB. This implies that the
810 fluid in the near-bed flow zone of the WGB accelerates more than that of the SGB owing to an
811 inrush of fluid parcels, resulting in a larger DA streamwise velocity. The spatial velocity
812 fluctuations in both the beds were plotted. In the near-bed flow zone, the data plot clusters
813 formed pseudo-elliptical shapes. The clusters became small beyond the roughness layer,
814 indicating the disappearance of spatial velocity fluctuations. The quadrant plots of spatial
815 velocity fluctuations in the WGB were more scattered than those in the SGB, indicating the
816 influence of differences between the roughness sizes of the two beds.

817 In this context, it is important to mention that the above results were obtained from the flow
818 measurements along the centerline of the flume. It is however acknowledged that the spanwise
819 roughness could afflict the DA flow results, if the streamwise roughness distributions at
820 spanwise locations (off the centerline) were different from that at the centerline of the flume, but
821 this was not the case for the beds studied, which was confirmed from the bed scanner results. In

823 that the streamwise roughness distributions at spanwise locations were approximately similar to
824 that at the centerline of the flume in both the beds.

825 In essence, the DAM experimental results allow us to clearly understand the impact of gravel-
826 bed roughness in WGBs and SGBs on the turbulent flow characteristics. This study reveals that
827 SGBs underestimate the turbulence parameters as compared to WGBs. Further, the WGB
828 preserves similar surface roughness organization and properties that are observed in a natural
829 gravel-bed river. To be explicit, (a) the vertical length scale of the roughness elements in a WGB
830 is less than half of the horizontal length scale of the roughness elements, (b) the gravels in the
831 WGB have a tendency to orient their longest axis in the streamwise direction, inducing the near-
832 bed flow to be relatively streamlined than that in the SGB, and (c) the higher spatial turbulent
833 stresses in the WGB than those in the SGB indicate that the favorable particle orientation and
834 direction of imbrication in the subsurface is to reduce the bulk porosity of the WGB. This
835 scenario closely resembles to the natural gravel-bed rivers. Thus, it can be concluded that in the
836 laboratory, the WGB is able to simulate, in a simplified manner, both the surface and subsurface
837 properties of a natural gravel-bed river. Hence, future experiments should be performed using
838 WGBs, as these are more representative of actual riverbed conditions. This would aid to produce
839 more accurate estimates of near-bed turbulence parameters. In contrast, near-bed turbulence
840 parameters obtained from experimental studies that use SGBs should be handled with care.

841 ¹ A. J. Grass, “Structural features of turbulent flow over smooth and rough boundaries,” *J. Fluid*
842 *Mech.* **50**, 233–255 (1971).

843 ² B. Kironoto and W. H. Graf, “Turbulence characteristics in rough uniform open-channel
844 flow,” *Proc. Inst. Civ. Eng. Water, Marit. Energy* **106**, 333–344 (1994).

845 ³ L. A. Giménez-Curto and M. A. Corniero, “Oscillating turbulent flow over very rough
846 surfaces,” *J. Geophys. Res.* **101**, 20745–20758 (1996).

847 ⁴ A. Dittrich and K. Koll, “Velocity field and resistance of flow over rough surface with large
848 and small relative submergence,” *Int. J. Sediment Res.* **12**, 21–33 (1997).

849 ⁵ V. Nikora and G. M. Smart, “Turbulence characteristics of New Zealand gravel-bed rivers,” *J.*
850 *Hydraul. Eng.* **123**, 764–773 (1997).

851 ⁶ V. Nikora and D. Goring, “Flow turbulence over fixed and weakly mobile gravel beds,” *J.*
852 *Hydraul. Eng.* **126**, 679–690 (2000).

853 ⁷ S. Dey and R. V. Raikar, “Characteristics of loose rough boundary streams at near-threshold,”
854 *J. Hydraul. Eng.* **133**, 288–304 (2007).

855 ⁸ S. Dey and R. Das, “Gravel-bed hydrodynamics: Double-averaging approach,” *J. Hydraul. Eng.*
856 **138**, 707–725 (2012).

857 ⁹ M. J. Franca and U. Lemmin, “Turbulence measurements in shallow flows in gravel-bed
858 rivers,” in *Proceedings of 7th International Conference Hydro-Science and Engineering*,
859 (Philadelphia, USA, 2006).

860 ¹⁰ J. F. Rodriguez and M. H. Garcia, “Laboratory measurements of 3-D flow patterns and
861 turbulence in straight open channel with rough bed,” *J. Hydraul. Res.* **46**, 454–465 (2008).

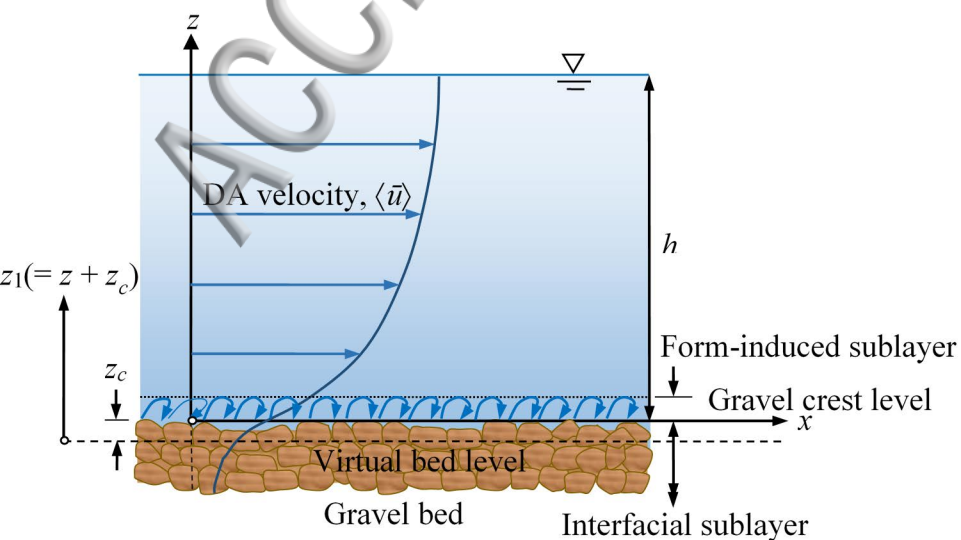
862 ¹¹ V. Nikora and P. M. Rowiński, “Rough-bed flows in geophysical, environmental and
863 engineering systems: Double averaging approach and its applications,” *Acta Geophys.* **56**,
864 529–934 (2008).

- 866 E. Mignot, E. Barthelemy, and D. Hurther, “Double-averaging analysis and local flow
867 characterization of near-bed turbulence in gravel-bed channel flows,” *J. Fluid Mech.* **618**,
868 279–303 (2009).
- 869 ¹³ E. Mignot, D. Hurther, and E. Barthelemy, “On the structure of shear stress and turbulent
870 kinetic energy flux across the roughness layer of a gravel-bed channel flow,” *J. Fluid*
871 *Mech.* **638**, 423–452 (2009).
- 872 ¹⁴ J. R. Cooper and S. J. Tait, “The spatial organization of time-averaged streamwise velocity and
873 its correlation with the surface topography of water-worked gravel beds,” *Acta Geophys.* **56**,
874 614–641 (2008).
- 875 ¹⁵ R. J. Hardy, J. L. Best, S. N. Lane, and P. E. Carbonneau, “Coherent flow structures in a depth-
876 limited flow over a gravel surface: The role of near-bed turbulence and influence of
877 Reynolds number,” *J. Geophys. Res.* **114**, F01003 (2009).
- 878 ¹⁶ J. R. Cooper and S. J. Tait, “Water-worked gravel beds in laboratory flumes—a natural
879 analogue?,” *Earth Surf. Processes Landforms* **34**, 384–397 (2009).
- 880 ¹⁷ K. Koll, S. J. Tait, J. Aberle, J. R. Cooper, S. J. McLelland, B. J. Murphy, and G. Massaro,
881 “Estimating flow turbulence characteristics over water-worked gravel beds using LDA and
882 PIV measurement systems,” in *Proceedings of International Conference on Fluvial*
883 *Hydraulics, River Flow* (Izmir, Turkey, 2008), Vol. 1, 739–746.
- 884 ¹⁸ K. Koll, J. R. Cooper, J. Aberle, S. J. Tait, and A. Marion, “Investigation into the physical
885 relationship between water-worked gravel bed armours and turbulent in-channel flow
886 patterns,” in *Proceedings of the HYDRALAB III Joint User Meeting* (Hannover, Germany,
887 2010).
- 888 ¹⁹ J. R. Cooper and S. J. Tait, “Spatially representative velocity measurement over water-worked
889 gravel beds,” *Water Resour. Res.* **46**, W11559 (2010).
- 890 ²⁰ J. R. Cooper and S. J. Tait, “Spatial variability in turbulent flows over water-worked gravel
891 beds,” in *Proceedings of International Conference on Fluvial Hydraulics, River Flow*
892 (Braunschweig, Germany, 2010), Vol. 1, pp. 51–58.
- 893 ²¹ J. R. Cooper, J. Aberle, K. Koll, and S. J. Tait, “Influence of relative submergence on spatial
894 variance and form-induced stress of gravel-bed flows,” *Water Resour. Res.* **49**, 5765–5777
895 (2013).
- 896 ²² S. J. McLelland, “Coherent secondary flows over a water-worked rough bed in a straight
897 channel,” in *Coherent Flow Structures at Earth’s Surface* (Chichester, UK, 2013), ISBN:
898 9781119962779.
- 899 ²³ S. Dey, *Fluvial Hydrodynamics: Hydrodynamic and Sediment Transport Phenomena*
900 (Springer-Verlag, Berlin, Germany, 2014).
- 901 ²⁴ V. Nikora, D. Goring, I. McEwan, and G. Griffiths, “Spatially averaged open-channel flow
902 over rough bed,” *J. Hydraul. Eng.* **127**, 123–133 (2001).
- 903 ²⁵ V. Nikora, K. Koll, I. McEwan, S. McLean, and A. Dittrich, “Velocity distribution in the
904 roughness layer of rough-bed flows,” *J. Hydraul. Eng.* **130**, 1036–1042 (2004).
- 905 ²⁶ V. Nikora, S. McLean, S. Coleman, D. Pokrajac, I. McEwan, L. Campbell, J. Aberle, D.
906 Clunie, and K. Koll, “Double-averaging concept for rough-bed open-channel and overland
907 flows: Applications,” *J. Hydraul. Eng.* **133**, 884–895 (2007).
- 908 ²⁷ V. Nikora, I. McEwan, S. McLean, S. Coleman, D. Pokrajac, and R. Walters, “Double-
909 averaging concept for rough-bed open-channel and overland flows: Theoretical
background,” *J. Hydraul. Eng.* **133**, 873–883 (2007).

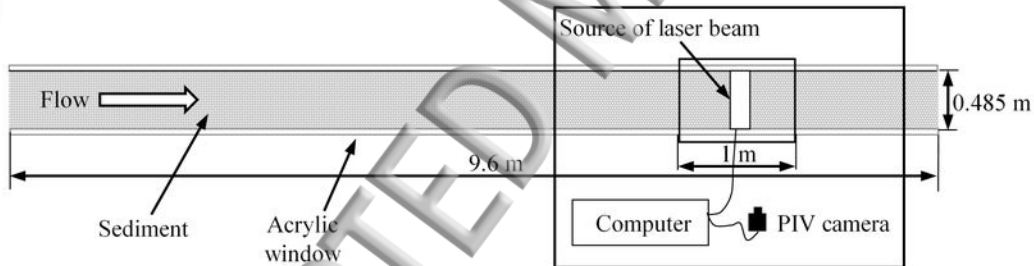
- 911 A. S. Monin and A. M. Yaglom, *Statistical Fluid Mechanics: Mechanics of Turbulence* (M.I.T
912 Press, Cambridge, 1971), Vol. I.
- 913 ²⁹ R. M. L. Ferreira, “Turbulent flow hydrodynamics and sediment transport: Laboratory
914 research with LDA and PIV,” in *Experimental Methods in Hydraulic Research*, edited by P.
915 Rowinski (Springer, Berlin, Heidelberg, 2011), Vol. I, pp. 67–111.
- 916 ³⁰ A. Melling, “Tracer particles and seeding for particle image velocimetry,” *Meas. Sci. Technol.*
917 **8**, 1407–1416 (1997).
- 918 ³¹ M. Raffel, C. E. Willert, S. T. Wereley, and J. Kompenhans, *Particle Image Velocimetry: A*
919 *Practical Guide* (Springer-Verlag, Berlin, Germany, 2007).
- 920 ³² C. Manes, D. Pokrajac, and I. McEwan, “Double-averaged open-channel flows with small
921 relative submergence,” *J. Hydraul. Eng.* **133**, 896–904 (2007).
- 922 ³³ C. Manes, D. Pokrajac, I. McEwan, and V. Nikora, “Turbulence structure of open channel
923 flows over permeable and impermeable beds: A comparative study,” *Phys. Fluids* **21**,
924 125109 (2009).
- 925 ³⁴ T. Buffin-Bélanger and A. Roy, “1 min in the life of a river: Selecting the optimal record
926 length for the measurement of turbulence in fluvial boundary layers,” *Geomorphology* **68**,
927 77–94 (2005).
- 928 ³⁵ M. Detert, V. Nikora, and G. H. Jirka, “Synoptic velocity and pressure fields at the water–
929 sediment interface of streambeds,” *J. Fluid Mech.* **660**, 55–86 (2010).
- 930 ³⁶ C. R. Neill, “Mean-velocity criterion for scour of coarse uniform bed material,” in *Proceedings*
931 *of International Association of Hydraulic Research 12th Congress* (Fort Collins, Colorado,
932 1967), Vol. 1, pp. 46–54.
- 933 ³⁷ V. I. Nikora, D. G. Goring, and B. J. Biggs, “On gravel-bed roughness characterization,”
934 *Water Resour. Res.* **34**, 517–527 (1998).
- 935 ³⁸ J. Aberle and G. M. Smart, “The influence of roughness structure on flow resistance on steep
936 slopes,” *J. Hydraul. Res.* **41**, 259–269 (2003).
- 937 ³⁹ G. M. Smart, M. J. Duncan, and J. M. Walsh, “Relatively rough flow resistance equations,” *J.*
938 *Hydraul. Eng.* **128**, 568–578 (2002).
- 939 ⁴⁰ S. Sarkar, A. N. Papanicolaou, and S. Dey, “Turbulence in a gravel-bed stream with an array of
940 large gravel obstacles,” *J. Hydraul. Eng.* **142**, 04016052 (2016).
- 941 ⁴¹ D. Ferraro, S. Servidio, V. Carbone, S. Dey, and R. Gaudio, “Turbulence laws in natural bed
942 flows,” *J. Fluid Mech.* **798**, 540–571 (2016).
- 943 ⁴² J. Aberle, “Measurements of armour layer roughness geometry function and porosity,” *Acta*
944 *Geophys.* **55**, 23–32 (2007).
- 945 ⁴³ D. Pokrajac, I. McEwan, and V. Nikora, “Spatially averaged turbulent stress and its
946 partitioning,” *Exp. Fluids* **45**, 73–83 (2008).
- 947 ⁴⁴ L. A. Giménez-Curto and M. A. Corniero, “Flow characteristics in the interfacial shear layer
948 between a fluid and a granular bed,” *J. Geophys. Res.* **107**, 1–12 (2002).
- 949 ⁴⁵ S. Sarkar and S. Dey, “Double-averaging turbulence characteristics in flows over a gravel
950 bed,” *J. Hydraul. Res.* **48**, 801–809 (2010).
- 951 ⁴⁶ I. Nezu and H. Nakagawa, *Turbulence in Open-Channel Flows* (International Association of
952 Hydraulic Engineering and Research Monograph, Rotterdam, Netherlands, 1993).
- 953 ⁴⁷ J. Aberle, K. Koll, and A. Dittrich, “Form induced stresses over rough gravel-beds,” *Acta*
954 *Geophys.* **56**, 584–600 (2008).
- 955 ⁴⁸ J. Yuan and U. Piomelli, “Roughness effects on the Reynolds stress budgets in near-wall
turbulence,” *J. Fluid Mech.* **760**, R1 (2014).

- 957 L. Prandtl, "Bericht über untersuchungen zur ausgebildeten turbulenz," Zeitschrift für
angewandte Mathematik und Mechanik **5**, 136–139 (1925).
- 958 ⁵⁰ S. S. Lu and W. W. Willmarth, "Measurements of the structures of the Reynolds stress in a
959 turbulent boundary layer," J. Fluid Mech. **60**, 481–511 (1973).

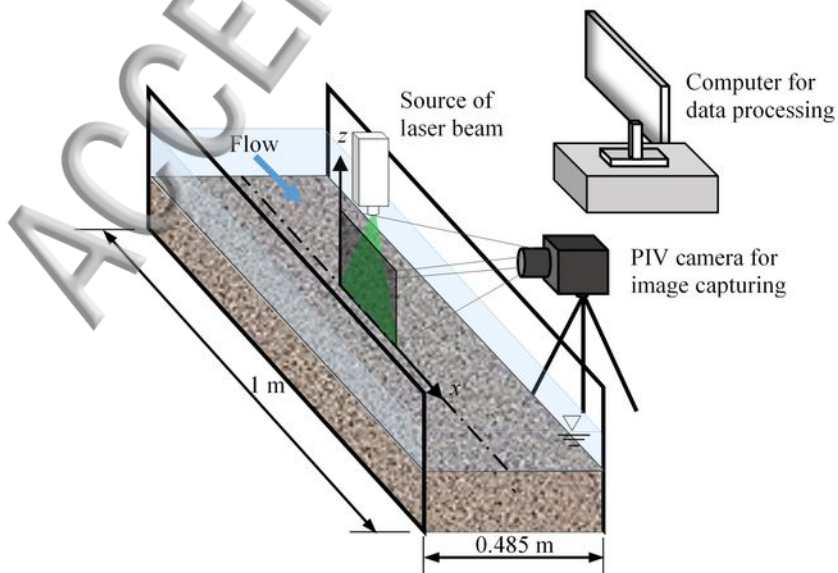
ACCEPTED MANUSCRIPT



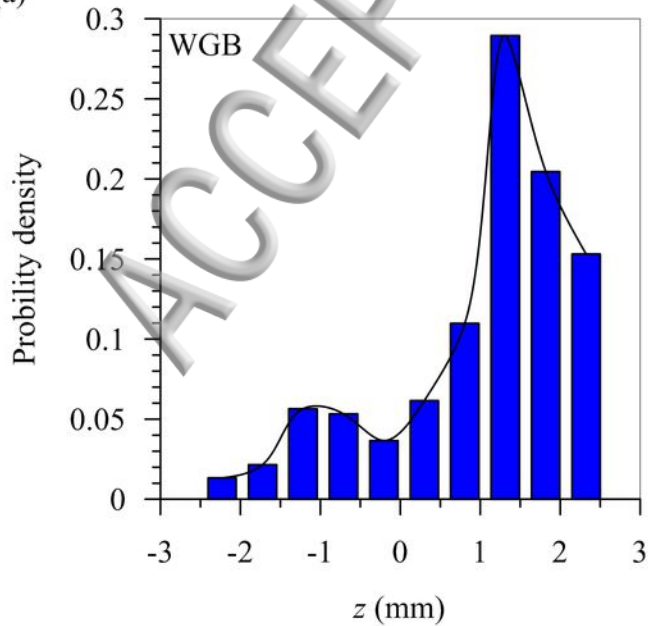
(a)



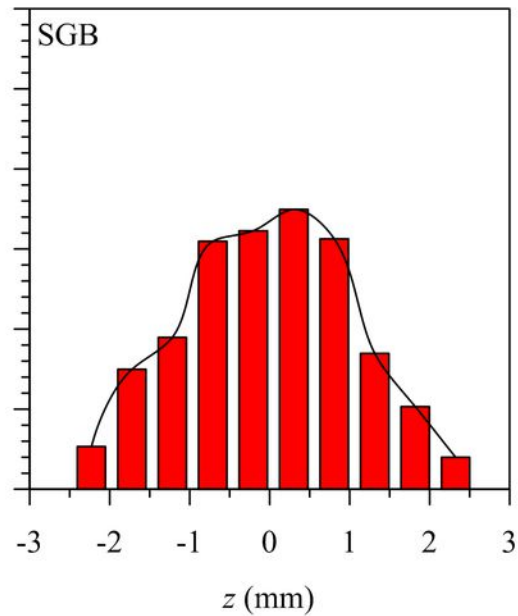
(b)

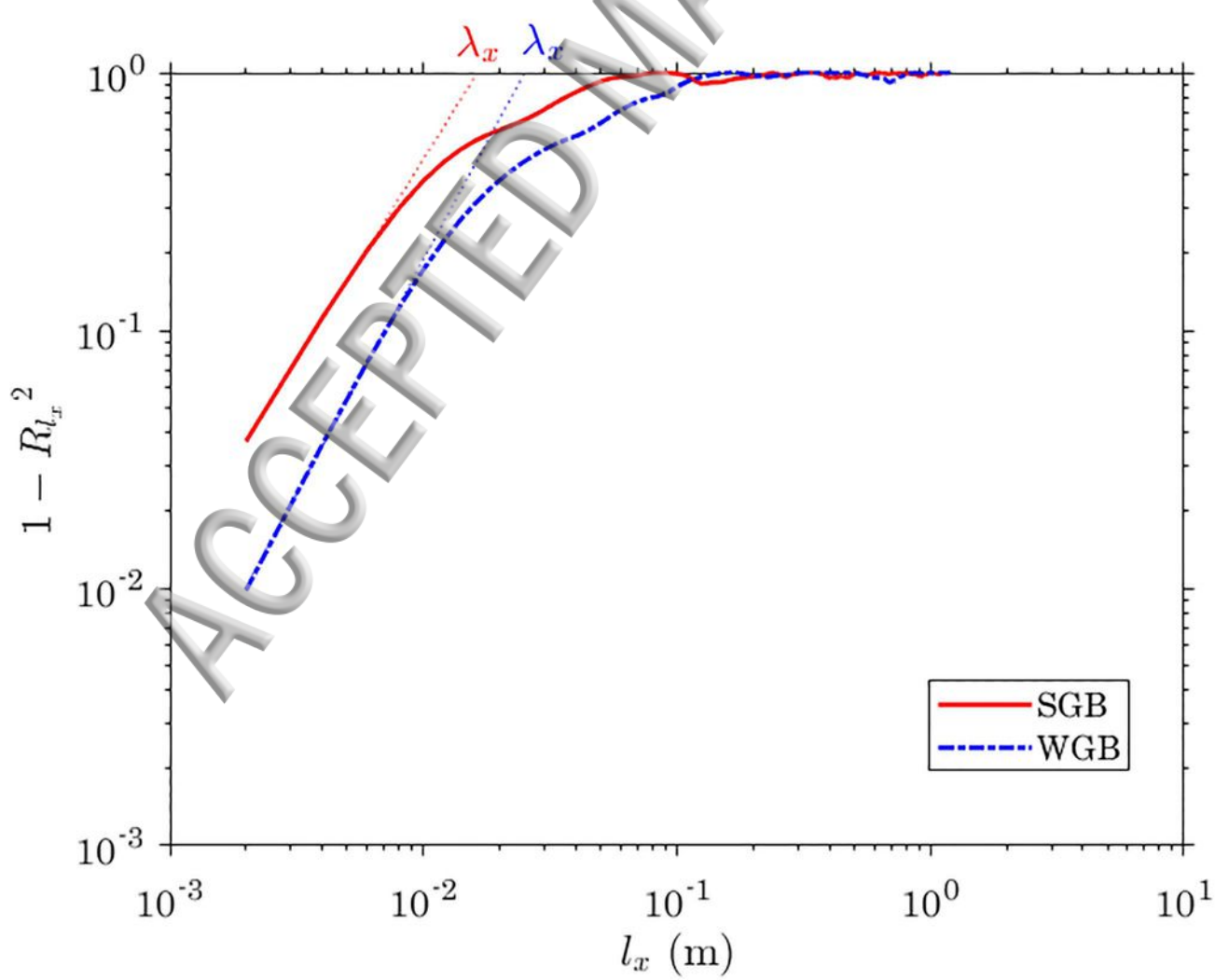


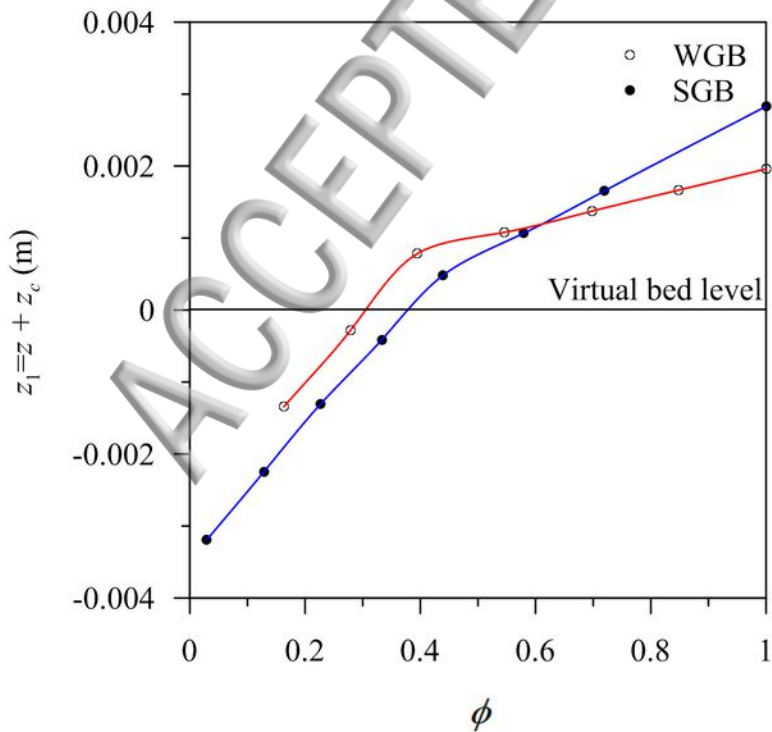
(a)

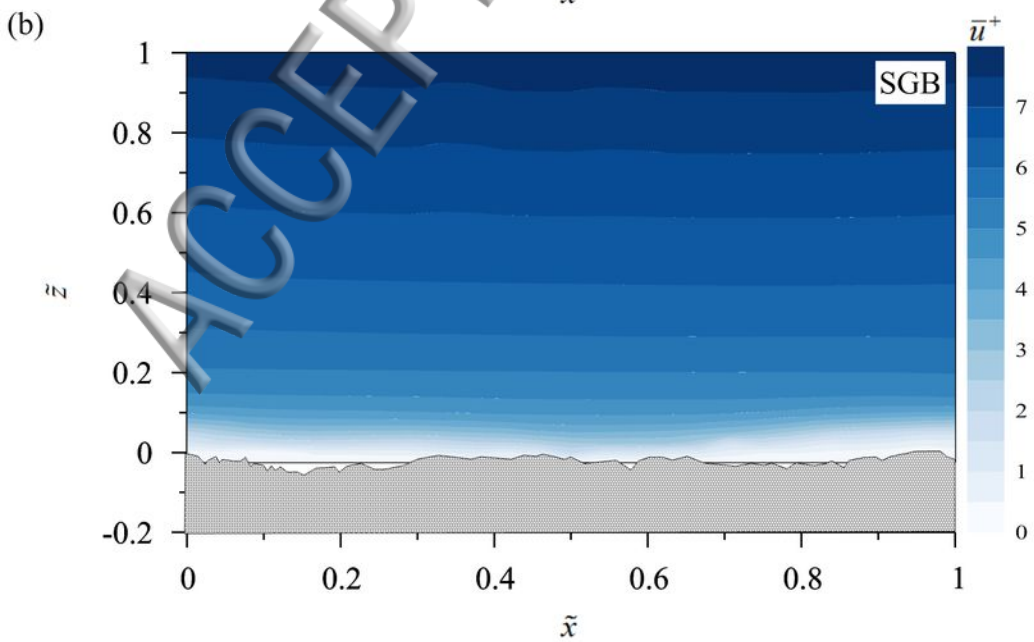
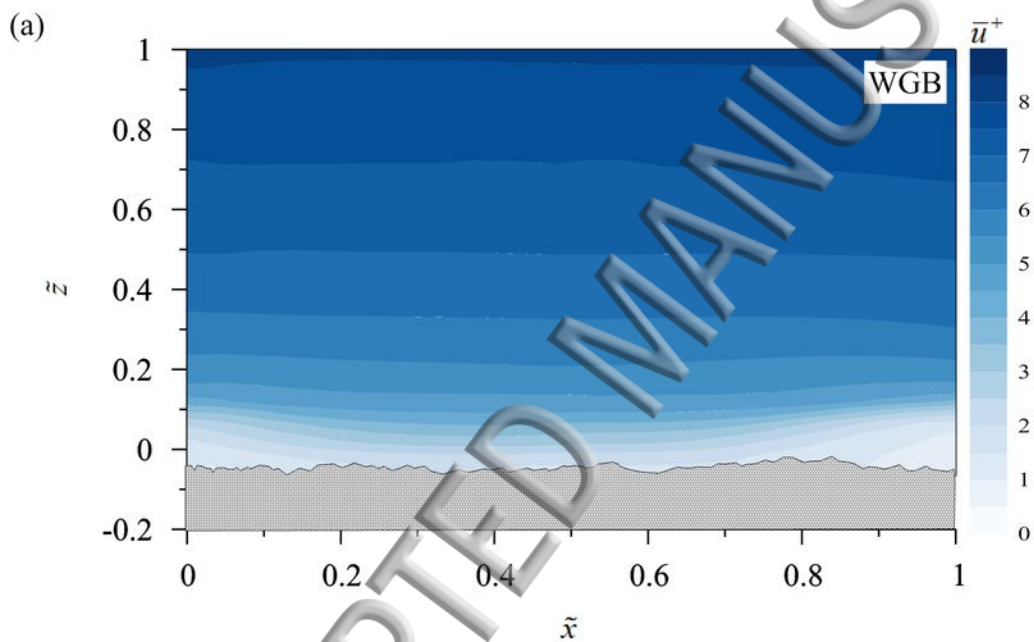


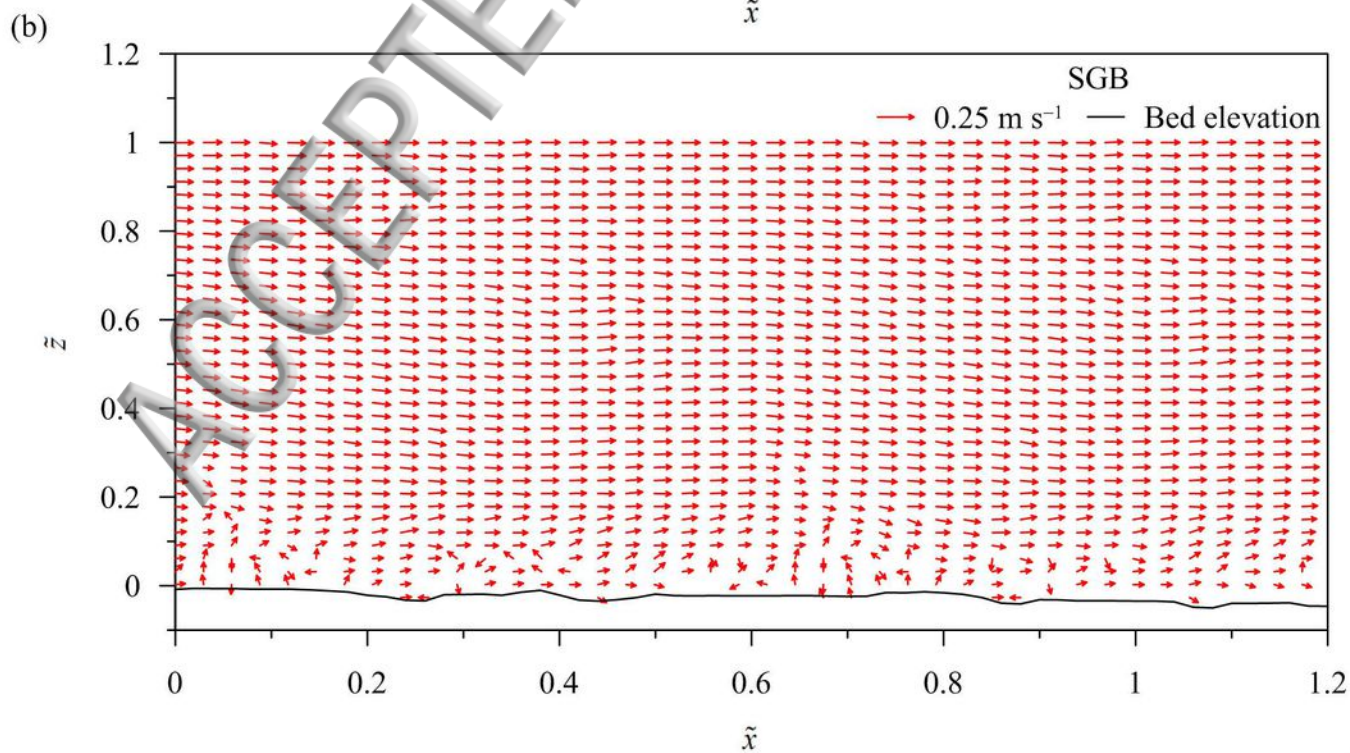
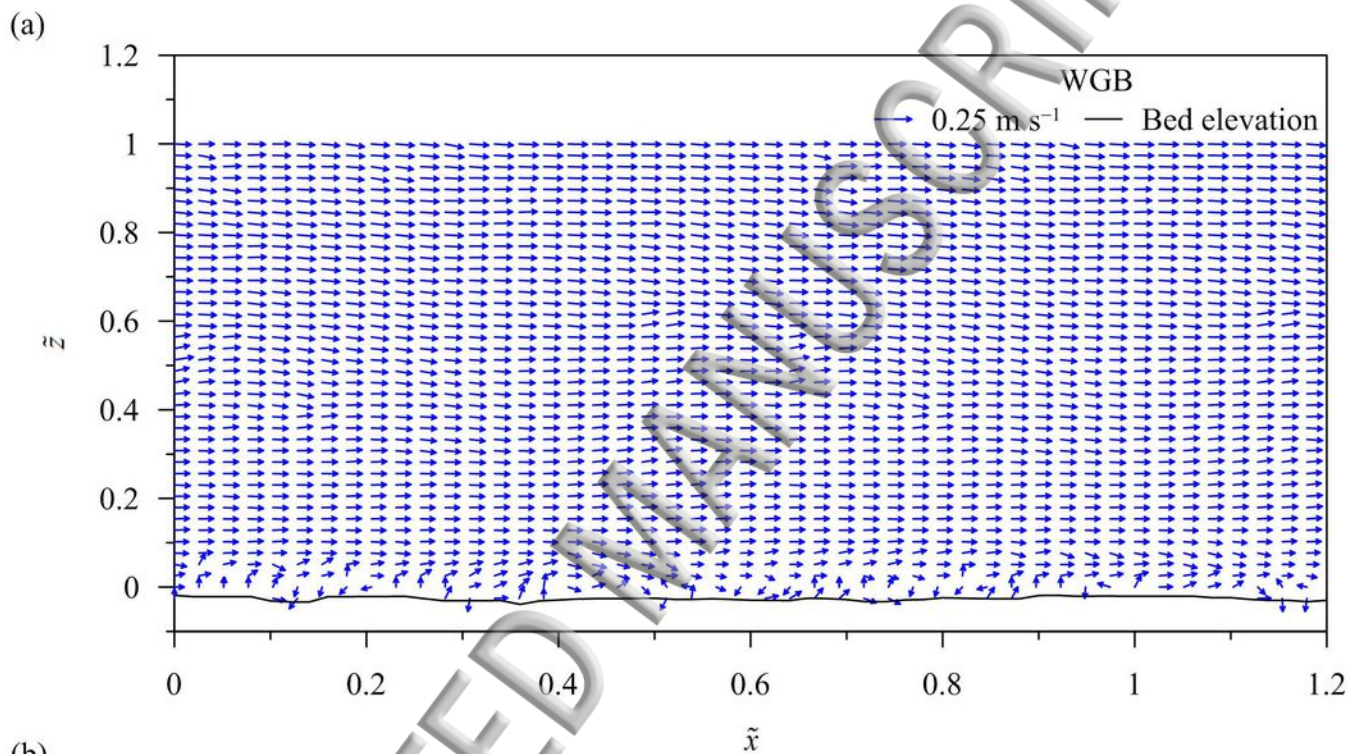
(b)

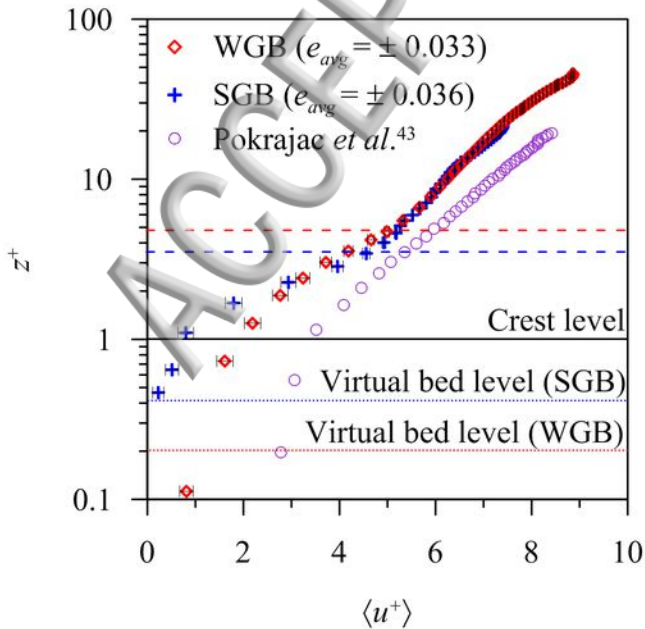




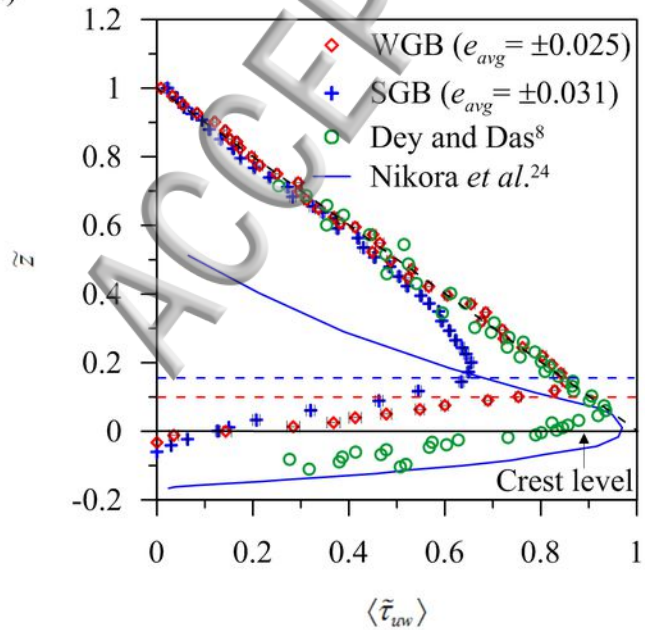




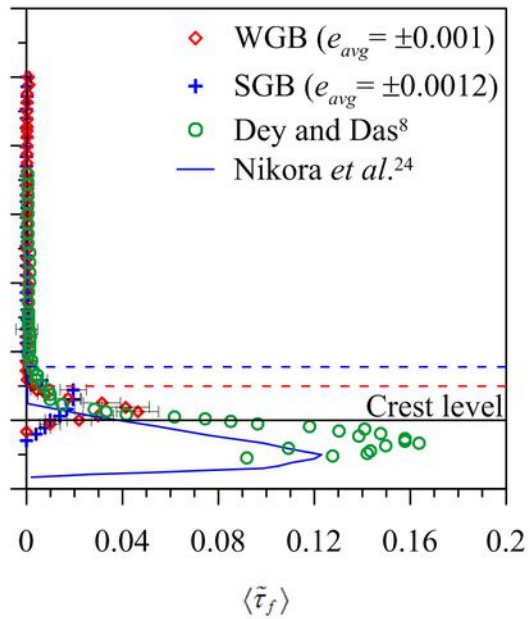


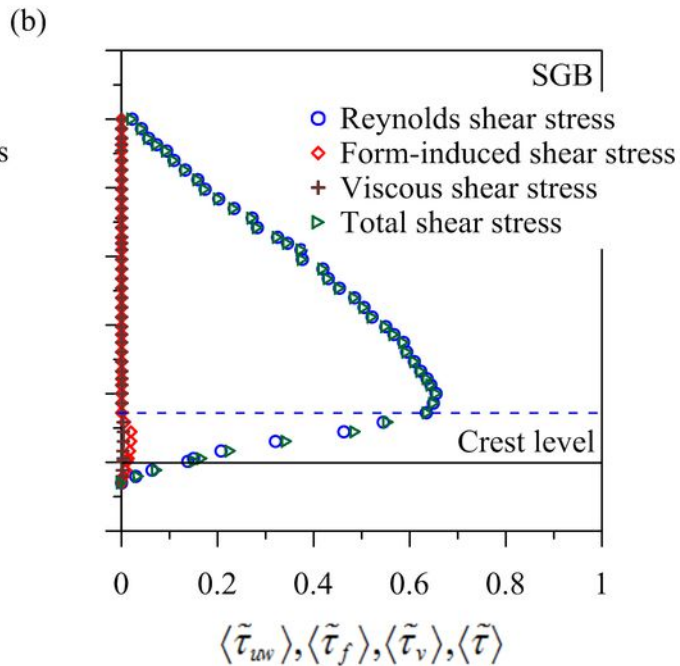
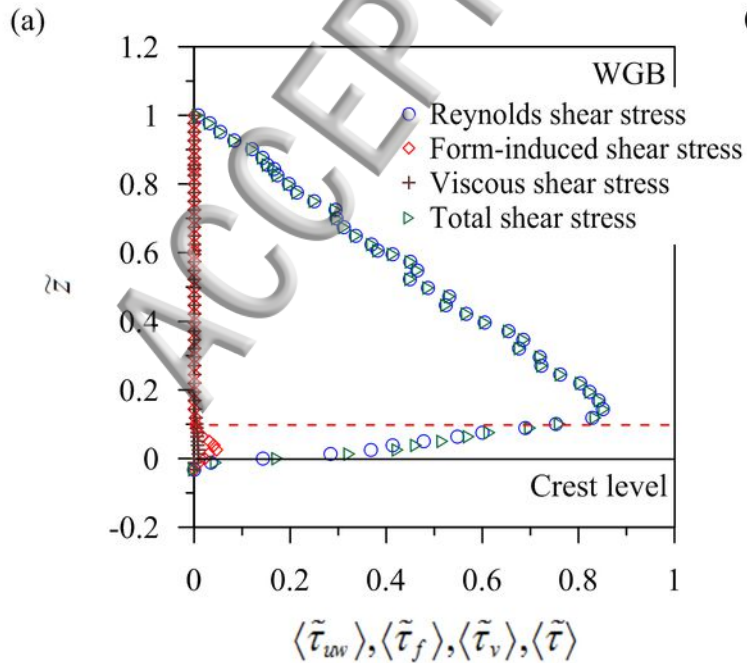


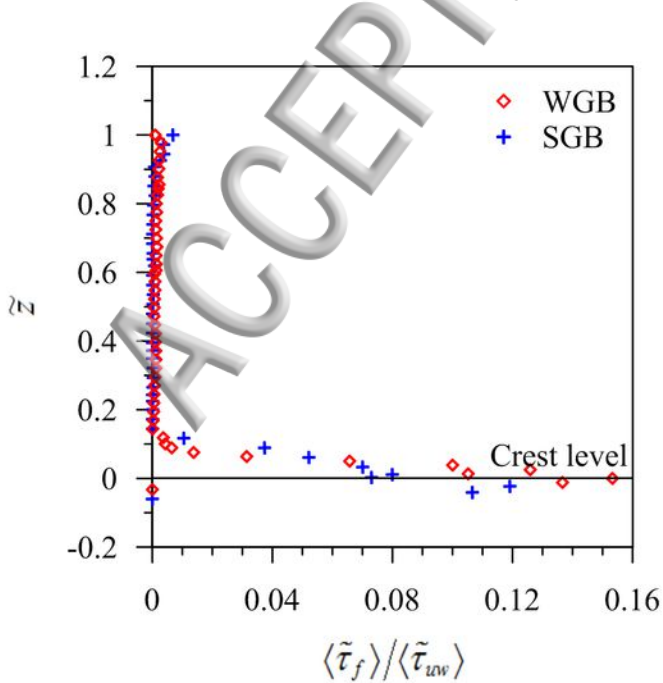
(a)

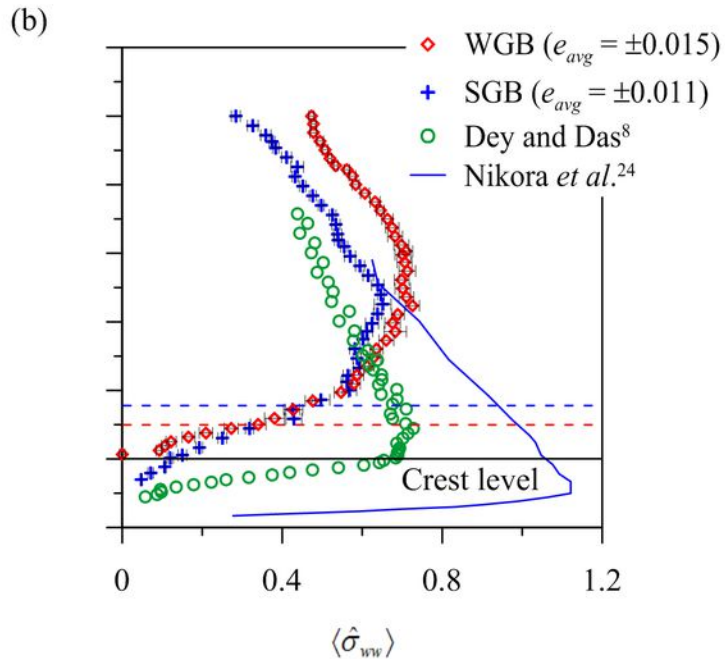
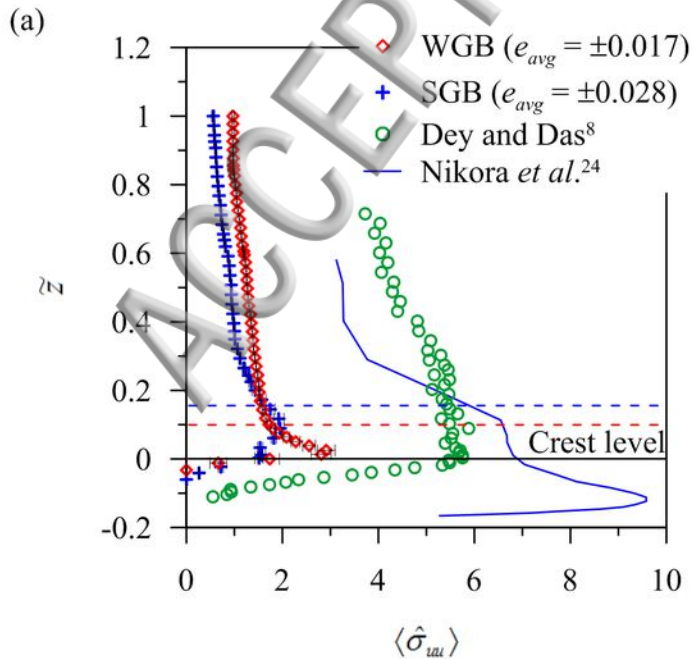


(b)

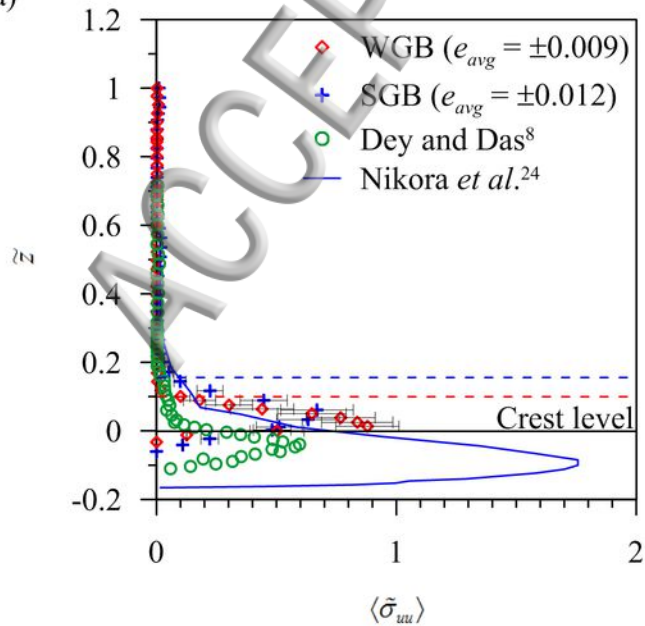




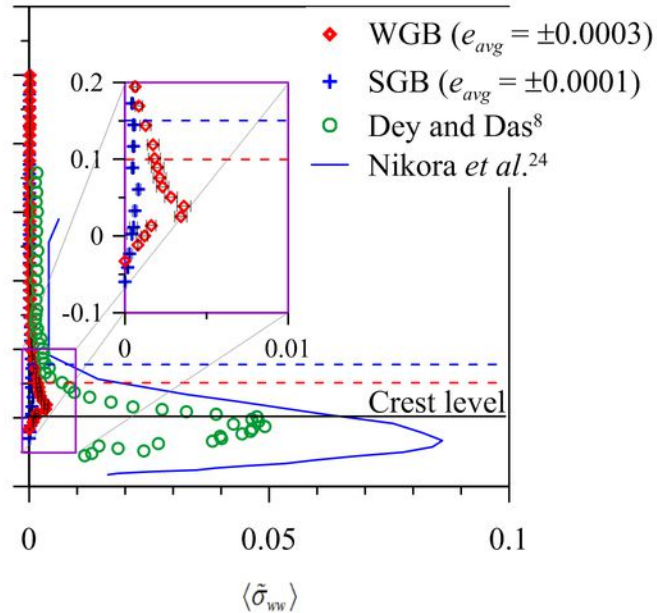


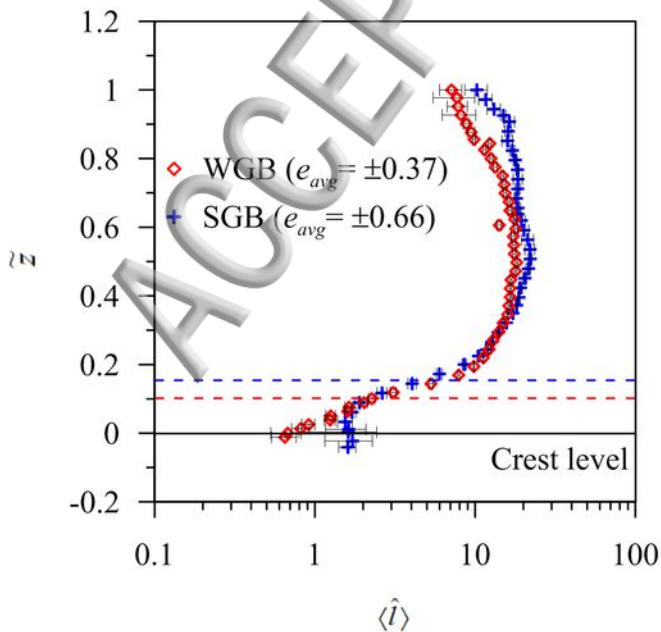


(a)

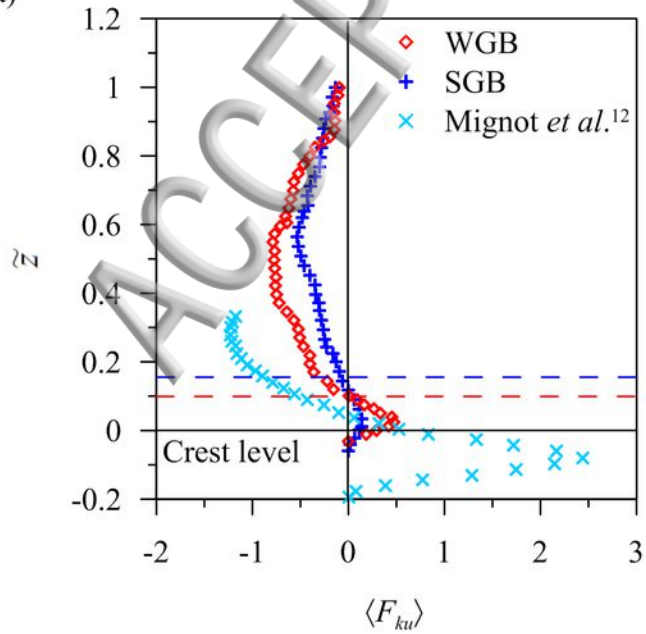


(b)

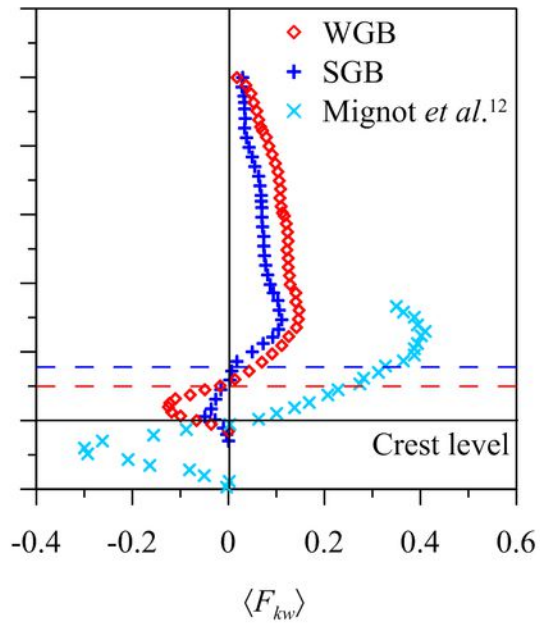




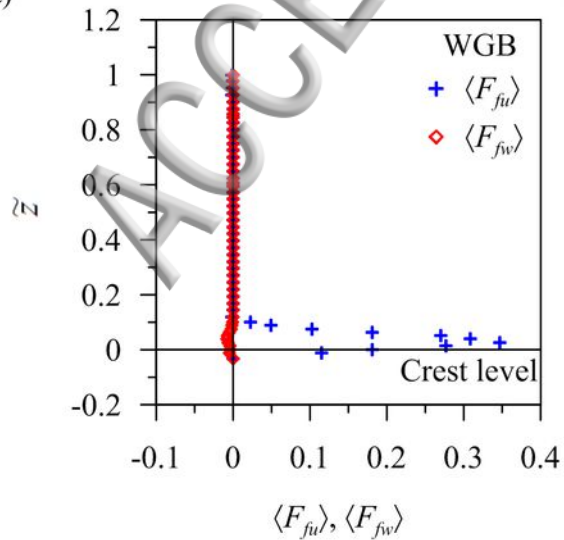
(a)



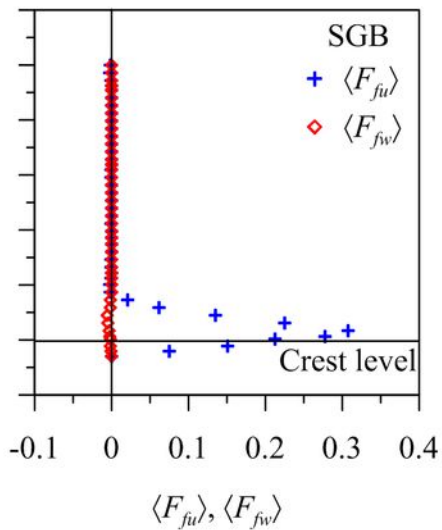
(b)



(a)



(b)



(c)

